Direct numerical simulations of turbulent periodic-hill flows with mass-conserving lattice Boltzmann method

Wei-Jie Lin,[1] Ming-Jiun Li,[1] Chi-Wei Su,[1] Xiao-Ying Huang,[1] and Chao-An Lin[1, a)]

Department of Power Mechanical Engineering, National Tsing Hua University, Hsinchu 30013, Taiwan

(Dated: 10 September 2020)

Multi-relaxation time lattice Boltzmann method is used to perform direct numerical simulations of laminar and turbulent pressure-driven flows within a channel with hill-shape periodic constriction for the first time. The simulations are conducted on graphics processing unit cluster with two-dimensional domain decomposition to accelerate the computation. The hill-shape boundary is represented using the interpolated bounce back scheme. However, the scheme generates mass leakage across the boundary, which is more pronounced in the turbulent flow regime, and this may produce diverging solutions for turbulent flows. The mass leakage due to the local mass imbalance along the curved boundary is solved by modifying the distribution functions locally or globally, and both predict similar velocity distributions. Since the global correction method is more computing time-consuming, the local correction method is adopted. The present numerical implementation's capability is first validated by performing direct numerical simulations of turbulent channel flow at $Re_\tau = 180$, and the current predicted results agree well with the benchmark solutions. Direct numerical simulations are further conducted for the turbulent flow over the periodic hill at $Re_h = 2800$. Both the mean velocity and turbulent stress compare favorably with the benchmark solutions. The present simulation also correctly predicts the turbulence splatting effect near the windward hill. Both phenomena are in good accordance with the benchmark solutions.

[a)] Electronic mail: calin@pme.nthu.edu.tw

I. INTRODUCTION

Lattice Boltzmann method (LBM) has been used as an alternative to the Navier-Stokes equation to simulate the dynamic, thermal, and two-phase flows[1–3]. Most applications focus on simple geometric flows at lower Reynolds numbers, because the mesh is in general uniform due to the Lagrangian discretization of the convective term[1]. Despite this limitation, the application of LBM to simulate turbulent flows were also actively pursued. Homogeneous isotropic box turbulence, for example, is frequently examined[4–6], where in general, the uniform mesh is adopted. LBM was demonstrated to generate compatible results with its Navier-Stokes equation-based counterpart, showing accurate energy spectrum distributions and energy decay.

Further, it would be desirable to perform LBM simulations of wall-bounded turbulent flows. A typical flow examined is the pressure-driven turbulent channel flows and is used as test cases to explore the validity of LBM studies. The predicted results were shown to reproduce the Navier-Stokes DNS data[7], though the investigated Reynolds number is generally low, such as at $Re_\tau = 180$[8–11]. For higher Reynolds number flows, the van Driest damping function and wall function were adopted to overcome the low near-wall grid resolution of turbulent wall-bounded flows[12,13]. Alternatively, Wu et al.[14] adopted the block-mesh refinement[15] to simulate turbulent channel flows up to Re_τ =640, where a successive grid-refinement resolved the wall layer toward the wall.

On the other hand, turbulent flows along curved surfaces with favorable or adverse pressure gradients are also frequently investigated. To mimic the complex geometry within the Cartesian mesh, several strategies have been proposed[15–18]. For example, Chen et al.[16] extended the extrapolation scheme to curved boundary using the castellated approach. Filippova and Hanel[15] proposed a method using simple linear interpolation between a fictitious equilibrium distribution function and a well-chosen near-boundary distribution function. The weighting factor of the interpolation is determined by the distance between the boundary and the near-boundary lattice. Mei et al.[17] further improved its numerical stability. Bouzidi et al.[19] proposed the interpolated bounce back scheme, where again, the interpolation is based on the wall distance parameter. Lallemand and Luo[18] combined the bounce-back scheme and interpolation scheme to treat a moving curved boundary by the lattice Boltzmann method. This treatment is an extension of that proposed by Bouzidi et al.[19]. An alternate approach was proposed by Lin and his co-workers[2,20], where a force like corrector was adopted to enforce the momentum and energy on the boundary nodes.

However, Lallenmand and Luo[21] indicated that the interpolation-based schemes destroy the mass conservation near the boundary. Thus, several mass conserving schemes have been proposed[22–24]. Further, Sanjeevi et al.[24] performed a systematic study to examine the degree of mass leakage over the curved boundary. It was found that the currently available schemes do not conserve mass over the curved boundary. The mass leakage is even more pronounced when the Reynolds number is high, and different mass conserving strategies were proposed[24]. However, the Reynolds number explored in previous studies[15–19,22–24] are still in the laminar flow regime.

The aim of the present study is to simulate turbulent wall bounded flows with extensive separation over curved surface using LBM. Flow separation due to the adverse pressure gradient has been the focus of studies, which can be caused by the abrupt change of the geometry[25–27], or the smoothly expanding boundary[28]. In particular, the recirculation induced by the gradual expanding-geometry along the curved surface is challenging to predict because the separating point can not be determined in advance, and the related research has been actively pursued. Thus, turbulent flow over periodic hills has been studied experimentally and numerically[28–31] due to the existence of complex flow patterns such as separation, recirculation, and reattachment. However, to the knowledge of the authors, LBM based direct numerical simulations (DNS) of turbulent periodic-hill flows are not available. In the present study, the focus is to perform direct numerical simulations of turbulent periodic-hill flow with a multi-relaxation time lattice Boltzmann method. The boundary condition is implemented using the scheme by Bouzidi et al.[19] with mass correction strategies[24]. There are three issues to be addressed here, i.e., determining the appropriate driving force to achieve the desired Reynolds number, the extent of the mass leakage of the interpolated bounce back scheme without mass correction, especially for turbulent flows, and the influence of the mass correction schemes on the solutions. Finally, turbulent flow predictions are to be contrasted with the DNS data of Breuer et al.[30] to assess the effectiveness of the present implementations. The simulation is conducted on message passing interface (MPI)-based graphics processing unit (GPU) cluster[32,33]. The remainder of this paper is organized as follows: In Section II, the mathematical formulation of the method is introduced. Finally, section IV present the conclusion.

II. MATHEMATICAL FORMULATION

A. Multi relaxation time lattice Boltzmann model

The D3Q19 multi-relaxation-time (MRT) lattice Boltzmann method[1,34,35] can be expressed by collision and streaming steps, respectively as in the following:

$$f_i^+(\mathbf{x},t) = f_i(\mathbf{x},t) - M_{il}^{-1} S_{lj}[m_j(\mathbf{x},t) - m_j^{eq}(\mathbf{x},t)] + G_i(\mathbf{x},t)\Delta t \tag{1}$$

$$f_i(\mathbf{x}+\mathbf{e}_i\Delta t, t+\Delta t) = f_i^+(\mathbf{x},t) \tag{2}$$

where $\mathbf{M}^1$ is a matrix that transforms the distribution function f_i to the velocity moment, $m_j = M_{ji} f_i$. $\mathbf{S}^1$ is the relaxation time diagonal matrix, and G_i is the external forcing term.

Based on the particle distribution functions, the macroscopic density and velocity can be obtained as:

$$\sum_i f_i = \rho, \quad \sum_i f_i \mathbf{e}_i = \rho \mathbf{u} \tag{3}$$

The equilibrium moments m_i^{eq} and external force term G_i are determined as:

$$m_j^{eq} = M_{ji} \underbrace{w_i \rho [1 + \frac{3}{C^2}(\mathbf{e}_i \cdot \mathbf{u}) + \frac{9}{2C^4}(\mathbf{e}_i \cdot \mathbf{u})^2 - \frac{3}{2C^2}(\mathbf{u}\cdot\mathbf{u})]}_{f_i^{eq}}, \tag{4}$$

$$G_i = 3 w_i \rho \frac{\mathbf{e}_i \cdot \mathbf{F}}{C^2} \tag{5}$$

$C = \Delta x/\Delta t$ is the lattice speed, where Δx and Δt are the lattice width and time step, respectively. Here, $\Delta x = \Delta t$, i.e. $C = 1$ and $\mathbf{F}$ is set to be the pressure gradient along the streamwise direction.

The weighting coefficients w_i are respectively as, $w_0 = 1/3$, $w_{1-6} = 1/6$, and $w_{7-18} = 1/36$. The particle velocity $\mathbf{e}_i$ is defined as,

$$\mathbf{e}_i = \begin{cases} (0,0,0)C, & i = 0 \\ (\pm 1,0,0)C, (0,\pm 1,0)C, (0,0,\pm 1,0)C & i = 1 \sim 6 \\ (\pm 1,\pm 1,0)C, (\pm 1,0,\pm 1)C, (0,\pm 1,\pm 1,0)C & i = 7 \sim 18 \end{cases} \tag{6}$$

B. Boundary conditions

Along the boundary, due to the inward streaming operations, particle distribution function may originate from the undefined nodes external to the flow domain. Therefore measures have to be taken to prescribe these unknown particle distribution functions. For example, at the near boundary fluid nodes, i.e., solid circular nodes shown in Fig. 1, nodes A , B, C and $\mathbf{x}_{nw}$ have respectively three, one, two and three unknown distribution functions (vectors 1-9). Here nw denotes the near-wall fluid nodes. The solid square (X_w) is the intersection of the upstream link (dashed line) with the wall boundary of the respective unknown distribution function. For easy identification, the same color is applied for the wall node (X_w) and upstream link (dashed line) for the respective unknown distribution function.

Consider the near wall fluid node at X_{nw}. If the unknown distribution function is denoted as $f_p(\mathbf{x}_{nw}, t)$, then $f_{i\neq p}(\mathbf{x}_{nw}, t + \Delta t) = f^+_{i\neq p}(\mathbf{x}_{nw} - \mathbf{e}_i\Delta t, t)$ (Eq. 2). Also, the unknown distribution function is obtained by using the interpolated bounce back scheme proposed by Bouzidi et al.[19], which is based on a wall distance parameter defined as $q = |\mathbf{x}_{nw} - \mathbf{x}_w|/|\mathbf{e}_p\Delta t|$, where the respective wall locations are represented by the solid square symbols along the solid-fluid boundary shown in Fig. 1. Depending on the value of the parameter q, Bouzidi et al.[19] proposed that,

$$\begin{aligned} q < 0.5,\ f_p(\mathbf{x}_{nw}, t + \Delta t) &= (1 - 2q) f^+_{-p}(\mathbf{x}_{nw} + \mathbf{e}_p\Delta t, t) + 2q f^+_{-p}(\mathbf{x}_{nw}, t) \\ q \geq 0.5,\ f_p(\mathbf{x}_{nw}, t + \Delta t) &= (1 - \tfrac{1}{2q}) f^+_{p}(\mathbf{x}_{nw}, t) + \tfrac{1}{2q} f^+_{-p}(\mathbf{x}_{nw}, t) \end{aligned} \tag{7}$$

where $\mathbf{e}_{-p} = -\mathbf{e}_p$ shown in Fig. 1 and open circle ($\mathbf{x}_{nw} + \mathbf{e}_p$) is the second fluid node away from the wall.

For $q = 0.5$, the scheme recovers the halfway bounce back scheme of Ladd[36], and the mass is conserved. When $q \neq 0.5$, the interpolation does not guarantee the local mass conservation, i.e. $\Delta\rho(\mathbf{x}_{nw}) = \sum f^+_{-p}(\mathbf{x}_{nw}, t) - \sum f_p(\mathbf{x}_{nw}, t + \Delta t) \neq 0$. As suggested by Sanjeevi et al.[24], there are four possibilities that the imbalance can be added to the distribution function, i.e.,

$$f_0(\mathbf{x}_{nw}, t + \Delta t) = f^+_0(\mathbf{x}_{nw}, t) + \Delta\rho(\mathbf{x}_{nw}) \qquad (scheme - A) \tag{8}$$

$$f_i(\mathbf{x}_{nw}, t + \Delta t) = f_i(\mathbf{x}_{nw}, t + \Delta t) + w_i\Delta\rho(\mathbf{x}_{nw}) \qquad (scheme - B) \tag{9}$$

$$f_0(\mathbf{x}_f, t + \Delta t) = f^+_0(\mathbf{x}_f, t) + \frac{\sum \Delta\rho(\mathbf{x}_{nw})}{N_f} \qquad (scheme - C) \tag{10}$$

$$f_i(\mathbf{x}_f, t + \Delta t) = f_i(\mathbf{x}_f, t + \Delta t) + w_i\frac{\sum \Delta\rho(\mathbf{x}_{nw})}{N_f} \qquad (scheme - D) \tag{11}$$

where N_f is the number of fluid nodes. For Eqs. 8 and 9, the corrections are added to the local nodes and for Eqs. 10 and 11, the corrections are distributed to all the fluid nodes. The influences of adopting Eqs. 8 to 11 on the solutions will be explored in the results section.

III. RESULTS

A. Turbulent channel flow

The numerical procedure is first validated by predicting the turbulent channel flow at $Re_\tau(u_\tau\delta/\nu)$=180, where the computational domain is $12\delta \times 2\delta \times 4.5\delta$ in the streamwise, vertical and spanwise directions, respectively. Two grid densities are adopted, i.e., $576 \times 96 \times 288$ and $1152 \times 192 \times 576$ with corresponding grid densities being Δ^+=3.8 and 1.9. Since a halfway bounce-back is adopted, therefore, the first grid point is located at y^+=1.9 and 0.95. Fig. 2(a) shows the predicted velocity distributions compared with the results of Moser et al.[7], where compatible results are predicted, though a slight deviation is observed using the $576 \times 96 \times 288$ grids. Similar results can be observed in the turbulence intensity predictions, shown in Fig. 2(b).

B. Flows over periodic hill

Here, the focus is on the predictions of flow over the periodic hill. Fig. 3 shows the geometry of the periodic hill, and the height of the domain is 3h, instead of the commonly used, 3.036h[29,30]. For turbulent flow, the width in the spanwise direction is chosen to be 4.5h[29,30] and for laminar flow the width is 2.25h. The boundary condition is implemented using the scheme by Bouzidi et al.[19] with mass correction[24], and for the straight boundary, q is 0.5, i.e., halfway bounce back. The Reynolds number is defined based on the bulk velocity at the hillcrest and the hill height ($U_{bc}h/\nu$), which is half of the Reynolds number based on the height of the flow passage. When simulating flows over the periodic hill, there are three issues to be addressed, i.e., determining the appropriate driving force to achieve the desired Reynolds number, the extent of the mass leakage of the interpolated bounce back scheme without mass correction, especially for turbulent flows, and finally the influence of the mass correction schemes on the solutions. Finally, turbulent flow predictions are to be contrasted with the DNS data of Breuer et al.[30] to assess the effectiveness of the present implementations.

1. *Determination of driving force*

For the periodic-hill geometry considered, there is no analytic solution of the driving force to reach the expected Reynolds number. Here, a similar measure as in Hsu et al.[37] is adopted. To achieve the desired bulk velocity the driving force is adjusted via the following formula, i.e.,

$$F^{IN_t} = F^{(I-1)N_t} + \beta\rho(U_{ref} - U_b^{IN_t-1})\frac{U_{ref}}{L}, \qquad I = 1, 2, 3, ... \tag{12}$$

where $\beta = max(0.001, \alpha/Re_h)$. N_t is the interval of the time step for force adjustment, which is adopted as 10,000. Thus, the force is updated every 10,000 steps ($\sim 0.67\ L/U_{ref}$-flow through time) to avoid generating new disturbance, especially at high Reynolds number flows. U_{ref} and $U_b(t)$ are the target bulk velocity and the predicted bulk velocity at the hillcrest. Here, $U_{ref} = U_{bc}$. The value of α investigated ranges from 3 to 14. Eq. 12 is applied to compute laminar and turbulent flows at Reynolds numbers being 100 and 2800, respectively. The mass conserved scheme adopted is scheme-A of Eq. 8.

Fig. 4 shows the time history of the predicted bulk velocity variations ($U^* = U_b(t)/U_{ref}$) with the force adjusted with Eq. 12 for laminar flow at Re=100 using α=10. The simulation saturates to the desired bulk velocity monotonically. For turbulent flow, such as at Re=2800, results using α =3 and 14 produce similar results. Fig. 5 shows the time variations of the force and bulk velocity for turbulent flow at Re=2800 with $\alpha = 14$. The predicted bulk velocity oscillates around the target velocity, resulting from the compensating force adjustment and the internal flow instability. After a few transients ($\sim$ 200 flow-through time), the velocity is time-averaged. As shown in Fig. 5, the time-averaged bulk velocity approaches the designated bulk velocity as time proceeds. The time-averaged period is approximately 700 flow-through time (U_{ref}/L).

2. *Mass leakage*

As indicated earlier, the original interpolated bounce back scheme by Bouzidi et al.[19] may cause mass leakage through the curved boundary[24]. For turbulent flows, this may lead to diverging solutions. Here, the influences with and without mass correction are explored, and the mass correction scheme adopted is scheme-A. Simulations are conducted for laminar flow (Re=100) and turbulent flows (Re=700 and 2800) and the results are shown in Figs. 6 and 7. For laminar flow at Re=100, as shown in Fig. 6, coarse grid generates higher degree of mass leakage. However, at 40 flow-through times, the mass leakages are around 2%, 0.4% and 0.00001% respectively for 144×48, 288×96 grid and 576×192 grids. For turbulent flows, the mass correction is more influential, as shown in Fig. 7. The mass leakages at 40 flow-through times are 0.25% and 2.5%, respectively, for Re=700 and 2800. For flow at Re=2800, simulation with the original interpolated bounce back scheme is unstable and prone to diverge as time progresses.

3. *Influences of mass correction schemes*

Here, to save computational time, the influence of the correction schemes, i.e., Eqs. 8 to 11 on the solutions are explored first for laminar flow at Re=100 using 576×192 grid. Figs. 8(a) to 8(c) show the predicted velocity and pressure distributions at eight selected locations.. The deceleration and acceleration of the flow due to the hill's presence is clearly observed and its associated decrease or rise of the predicted pressure levels. No perceivable difference is observed using the four schemes at such a fine grid, even for the vertical velocity, which is relatively smaller than the streamwise velocity.

Zoomed views of the pressure contours at the windward hill are shown in Fig. 9, where results using scheme-A and scheme-C are presented. At two to three grid spacing above the hill boundary, the predicted contours are similar. However, using scheme-A, there is a local increase in the pressure level near the boundary, whereas scheme-C generates smoother results. These are consistent with those observed in Sanjeevi et al.[24]. It should be further noted here that schemes (A) and (B) show a similar rise in the local pressure distributions at the windward hill. The pressure distributions using schemes (C) and (D) are identical and do not show such a local rise of pressure at the corresponding region. Despite this deficiency, predicted velocity distributions are exactly the same using the four schemes. For the lines representing different schemes collapse and the difference can not be observed, as shown in the zoomed view of the velocity contours shown in Fig. 10.

Figs. 11 and 12 show the predicted mean and turbulent quantities at Re=2800 using scheme-A and C. Again, no perceivable differences are observed among the results. Since, Eqs. 10 and 11 requires global operations, and are thus time consuming compared to Eqs. 8 and 9, therefore, in subsequent simulations, Scheme-A is adopted for simplicity.

4. Turbulent periodic-hill flow at Re=2800

Here, the focus is to validate the turbulent periodic-hill flow predictions using the direct numerical simulation data of Breuer et al.[30], where the numerical procedure is based on the Navier-Stokes equation using curvilinear grid discretized with the second-order accurate scheme. The adopted Reynolds number based on the bulk velocity U_b and hill height h is 2800. The computational domain is shown in Fig. 3. Here, the mass conservation scheme-A is adopted for simplicity. The grids adopted in the streamwise, vertical and spanwise directions are $576 \times 192 \times 288$ and $864 \times 288 \times 432$. Since two grids generate compatible results (not shown here), $864 \times 288 \times 432$ grid is used. Also, H=3.036h is also adopted in the simulations using $864 \times 292 \times 432$ grid to examine the influence of the height on the solution.

Fig. 13 shows the predicted mean velocity distributions at ten selected locations, and the results are contrasted with the DNS data of Breuer et al.[30]. The usage of H=3h as height causes a slight departure from the benchmark solution of the mean streamwise velocity distributions shown in Fig. 13(a) in the region near the top boundary, and the simulated results using 3.036h agree quite well with the benchmark solutions. Despite the slight difference of the adopted height, the predicted results agree quite well with Breuer et al. 's DNS data for both the streamwise and vertical velocity components. The shear layer and recirculation zone are predicted well by the present scheme. The top boundary's height has a marginal impact on the bottom wall-flow, and this was also observed by Fröhlich et al.[29].

Figs. 14(a)-14(c) and 14(d) show respectively the predicted turbulence intensities and shear stresses. Apart from the slight deviation of the predicted turbulence intensity near the top boundary due to the different height adopted, in general, the agreements are good.

The rise of the turbulence level near the shear layer at the height of the hillcrest is also in accordance with the DNS data of Breuer et al.[30]. The rise of the bottom wall spanwise turbulence intensity at x/h=8, which is greater than the corresponding streamwise turbulence intensity, is due to the pressure strain-induced splatting effect[29] resulting from the presence of the windward hill.

IV. CONCLUSION

Turbulent pressure-driven flows within a channel with hill-shape periodic constriction are simulated with multi-relaxation time lattice Boltzmann method on GPU cluster. A methodology is proposed to determine the appropriate driving force to achieve the desired Reynolds number. The hill-shape boundary is mimicked by the interpolated bounce back scheme by Bouzidi et al.[19]. However, the scheme generates mass leakage across the boundary, which is more pronounced in the turbulent flow regime, and this may produce diverging solutions for turbulent flows. The mass leakage due to the local mass imbalance along the curved boundary is solved by modifying the distribution function locally or globally, as suggested by Sanjeevi et al.[24]. The locally modified method produces a slight increase in pressure locally in contrast to the global correction methods. On the other hand, the mass correction strategies marginally influence the predicted velocity distributions. Since the global correction method is more computing time-consuming, the local correction method is adopted. The capability of the present numerical implementation is first validated by performing direct numerical simulations of turbulent channel flow at $Re_\tau = 180$, and the current predicted results agree well with the benchmark solution by Moser et al.[7]. Direct numerical simulations of turbulent flow over the periodic hill are conducted at $Re_h = 2800$, and the predicted results are contrasted with the DNS data of Breuer et al[30]. Both the mean velocity and turbulent stress compare favorably with the benchmark solutions. The present simulation also correctly predicts the turbulence splatting effect, i.e., spanwise turbulence intensity being higher than the corresponding streamwise turbulence intensity, resulting from the windward hill's presence. Both phenomena are in good accordance with the DNS data by Breuer et al.[30].

ACKNOWLEDGEMENTS

The authors gratefully acknowledge the supports by the Ministry of Science and Technology, Taiwan (Grant No. 105-2221-E-007-061-MY3) and the computational facilities provided by the Taiwan National Center for High-Performance Computing.

DATA AVAILABILITY STATEMENT

The data that support the findings of this study are available from the corresponding author upon reasonable request.

REFERENCES

[1] D. d'Humierès, I. Ginzburg, M. Krafczyk, P. Lallemand, and L.-S. Luo, "Multiple-relaxation-time lattice boltzmann models in three dimensions," Phil. Trans. R. Soc. A. **360**, 437 – 451 (2002).

[2] K.-H. Lin, C.-C. Liao, S.-Y. Lien, and C.-A. Lin, "Thermal lattice boltzmann simulations of natural convection with complex geometry," Computers and Fluids **69**, 35 – 44 (2012).

[3] A. Fakhari, M. Geier, and T. Lee, "A weighted multiple-relaxation-time lattice boltzmann method for multiphase flows and its application to partial coalescence cascades," Journal of Computational Physics **341**, 22 – 43 (2017).

[4] N. Satofuka and T. Nishioka, "Parallelization of lattice boltzmann method for incompressible flow computations," Computational Mechanics **23**, 164–171 (1999).

[5] H. Yu, S. S. Girimaji, and L.-S. Luo, "Lattice boltzmann simulations of decaying homogeneous isotropic turbulence," Phys. Rev. E **71**, 016708 (2005).

[6] W. A. Kareem, S. Izawa, A.-K. Xiong, and Y. Fukunishi, "Lattice boltzmann simulations of homogeneous isotropic turbulence," Computers and Mathematics with Applications **58**, 1055 – 1061 (2009).

[7] R. D. Moser, J. Kim, and N. N. Mansour, "Direct numerical simulation of turbulent channel flow up to ret=590," Physics of Fluids **11**, 943–945 (1999).

[8] P. Lammers, K. Beronov, R. Volkert, G. Brenner, and F. Durst, "Lattice bgk direct numerical simulation of fully developed turbulence in incompressible plane channel flow," Computers and Fluids **35**, 1137 – 1153 (2006).

[9]K. Suga, Y. Kuwata, K. Takashima, and R. Chikasue, "A d3q27 multiple-relaxation-time lattice boltzmann method for turbulent flows," Computers and Mathematics with Applications **69**, 518 – 529 (2015).

[10]Y. Koda and F.-S. Lien, "The lattice boltzmann method implemented on the gpu to simulate the turbulent flow over a square cylinder confined in a channel," Flow, Turbulence and Combustion **94**, 495–512 (2015).

[11]Y.-H. Lee, L.-M. Huang, Y.-S. Zou, S.-C. Huang, and C.-A. Lin, "Simulations of turbulent duct flow with lattice boltzmann method on gpu cluster," Computers and Fluids **168**, 14 – 20 (2018).

[12]K. N. Premnath, M. J. Pattison, and S. Banerjee, "Generalized lattice boltzmann equation with forcing term for computation of wall-bounded turbulent flows," Phys. Rev. E **79**, 026703 (2009).

[13]S. Wilhem, J. Jacob, and P. Sagaut, "An explicit power-law-based wall model for lattice boltzmann method-reynolds averaged numerical simulations of the flow around airfoils," Physics of Fluids **30**, 065111 (2018).

[14]C.-M. Wu, Y.-S. Zhou, and C.-A. Lin, "Direct numerical simulations of turbulent channel flows with mesh-refinement lattice boltzmann methods on gpu cluster," Computers and Fluids **210**, 104647 (2020).

[15]O. Filippova and D. Hanel, "Grid refinement for lattice-bgk models," Journal of Computational Physics **147**, 219–228 (1998).

[16]S. Chen, D. Martinez, and R. Mei, "On boundary conditions in lattice boltzmann methods," Physics of Fluids **8**, 2527–2536 (1996).

[17]R. Mei, L.-S. Luo, and W. Shyy, "An accurate curved boundary treatment in the lattice boltzmann method," Journal of Computational Physics **155**, 307–330 (1999).

[18]P. Lallemand and L.-S. Luo, "Lattice boltzmann method for moving boundaries," Journal of Computational Physics **184**, 406–421 (2003).

[19]M. Bouzidi, M. Firdaouss, and P. Lallemand, "Momentum transfer of a boltzmann-lattice fluid with boundaries," Physics of Fluids **13**, 3452 – 3459 (2001).

[20]C. Chang, C.-H. Liu, and C.-A. Lin, "Boundary conditions for lattice boltzmann simulations with complex geometry flows," Computers and Mathematics with Applications **58**, 940 – 949 (2009).

[21]P. Lallemand and L.-S. Luo, "Lattice boltzmann method for moving boundaries," Journal of Computational Physics **184**, 406 – 421 (2003).

[22]P.-H. Kao and R.-J. Yang, "An investigation into curved and moving boundary treatments in the lattice boltzmann method," Journal of Computational Physics **227**, 5671 – 5690 (2008).

[23]J. Bao, P. Yuan, and L. Schaefer, "A mass conserving boundary condition for the lattice boltzmann equation method," Journal of Computational Physics **227**, 8472 – 8487 (2008).

[24]S. K. P. Sanjeevi, A. Zarghami, and J. T. Padding, "Choice of no-slip curved boundary condition for lattice boltzmann simulations of high-reynolds-number flows," Phys. Rev. E **97**, 043305 (2018).

[25]B. F. Armaly, F. Durst, J. C. F. Pereira, and B. Schönung, "Experimental and theoretical investigation of backward-facing step flow," Journal of Fluid Mechanics **127**, 473–496 (1983).

[26]K. Basnet and G. Constantinescu, "The structure of turbulent flow around vertical plates containing holes and attached to a channel bed," Physics of Fluids **29**, 115101 (2017).

[27]K. Basnet and G. Constantinescu, "Effect of a bottom gap on the mean flow and turbulence structure past vertical solid and porous plates situated in the vicinity of a horizontal channel bed," Physical Review Fluids **4**, 044604 (2019).

[28]G. Almeida, D. Durao, and M. Heitor, "Wake flows behind two-dimensional model hills," Experimental Thermal and Fluid Science **7**, 87–101 (1993).

[29]J. Fröhlich, C. P. Mellen, W. Rodi, L. Temmerman, and M. A. Leschziner, "Highly resolved large-eddy simulation of separated flow in channel with streamwise periodic constriction," Journal of Fluid Mechanics **526**, 19–66 (2005).

[30]M. Breuer, N. Peller, C. Rapp, and M. Manhart, "Flow over periodic hills - numerical and experimental study in a wide range of reynolds numbers," Computers and Fluids **38**, 433–457 (2009).

[31]P.-H. Chang, C.-C. Liao, H.-W. Hsu, S.-H. Liu, and C.-A. Lin, "Simulations of laminar and turbulent flows over periodic hills with immersed boundary method," Computers and Fluids **92**, 233–243 (2014).

[32]P.-Y. Hong, L.-M. Huang, L.-S. Lin, and C.-A. Lin, "Scalable multi-relaxation-time lattice boltzmann simulations on multi-gpu cluster," Computers and Fluids **110**, 1 – 8 (2015).

[33] X. Shi, T. Agrawal, C.-A. Lin, F.-N. Hwang, and T.-H. Chiu, “A parallel nonlinear multigrid solver for unsteady incompressible flow simulation on multi-gpu cluster,” Journal of Computational Physics **414**, 109447 (2020).

[34] D. d’Humières, “Generalized lattice-boltzmann equationsd,” Prog. Aeronaut. Astronaut. **450-458**, 6546–6562 (1992).

[35] P. Lallemand and L.-S. Luo, “Theory of the lattice boltzmann method: Dispersion, dissipation, isotropy, galilean invariance, and stability,” Phys. Rev. E **61**, 6546–6562 (2000).

[36] A. J. C. Ladd, “Numerical simulations of particulate suspensions via a discretized boltzmann equation. part 1. theoretical foundation,” Journal of Fluid Mechanics **271**, 285 – 309 (1994).

[37] H.-W. Hsu, J.-B. Hsu, W. Lo, and C.-A. Lin, “Large eddy simulation of turbulent couette-poiseuille and couette flows inside a square duct,” Journal of Fluid Mechanics **702**, 89 – 101 (2012).

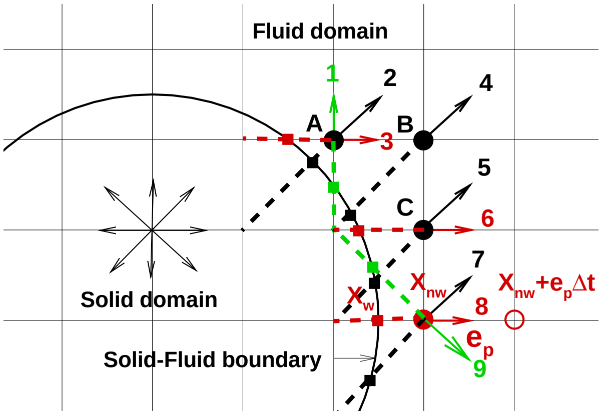

FIG. 1. Solid-fluid boundary treatment (solid square: wall boundary nodes associated with respective arrow; solid circle: near wall fluid node (A, B, C, X_{nw}); open circle: the second fluid node away from the wall; arrows (1-9): unknown distribution functions).

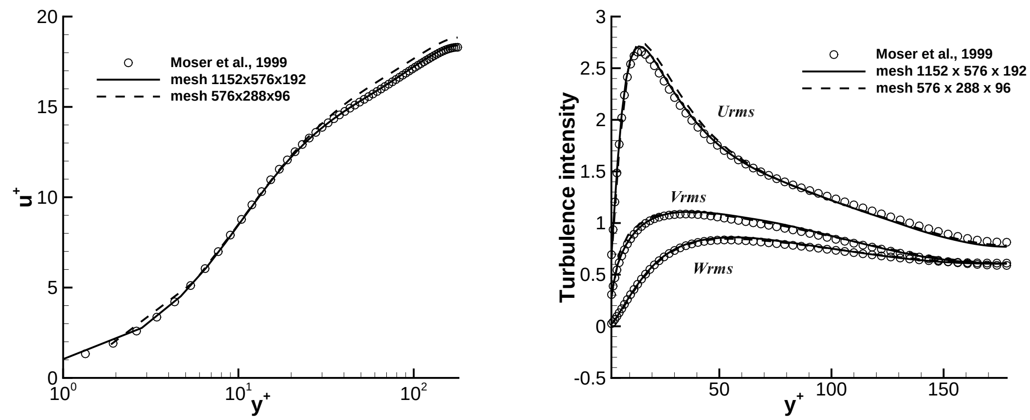

(a) (b)

FIG. 2. Predicted streamwise velocity and the turbulent intensities of channel flow at $Re_\tau = 180$. (a) Streamwise velocity, (b) Turbulence intensities.

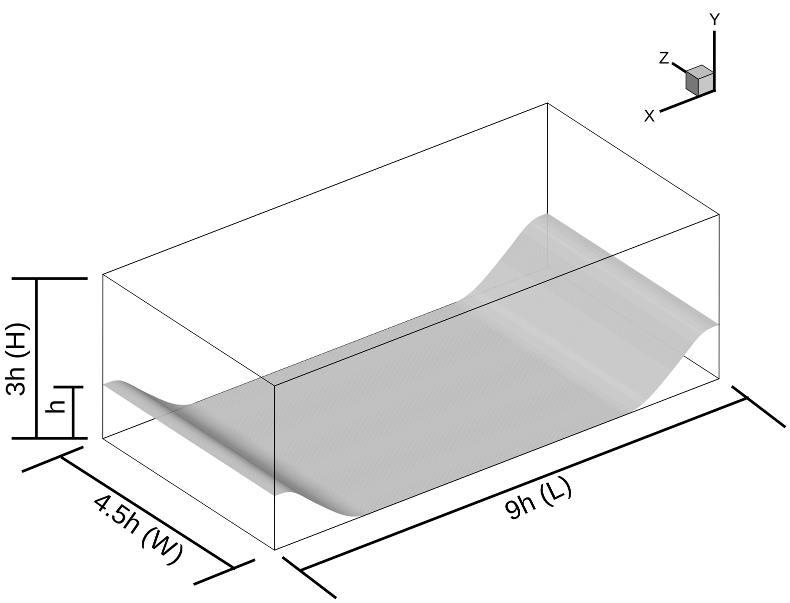

FIG. 3. The geometry of periodic hill.

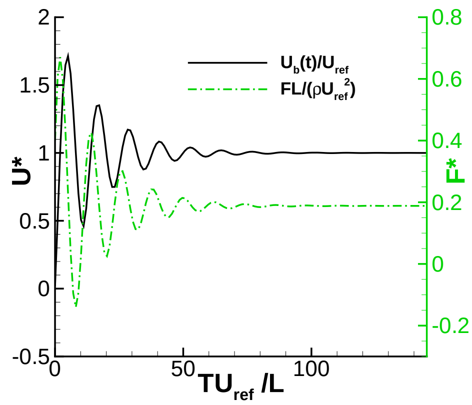

FIG. 4. Predicted bulk velocity and force variations (Re=100, 576 × 192 × 144 grid.)

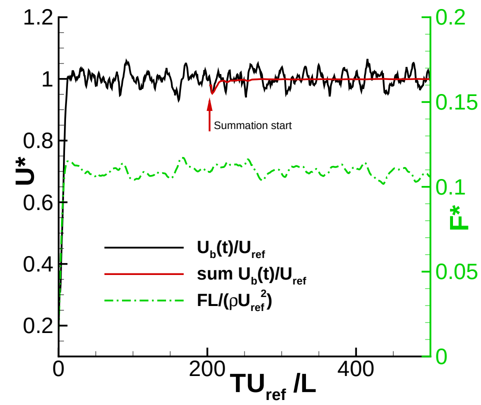

FIG. 5. Predicted bulk velocity and force variations (Re=2800, 864 × 288 × 432 grid.)

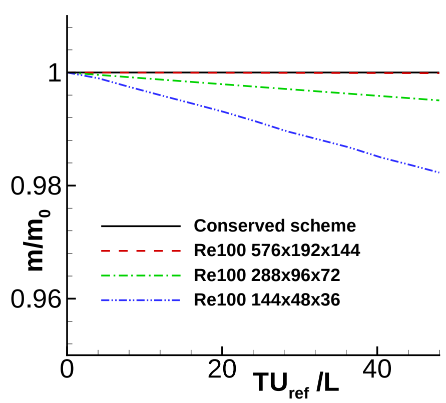

FIG. 6. Mass variations within the computational domain with and without mass correction (Re=100)

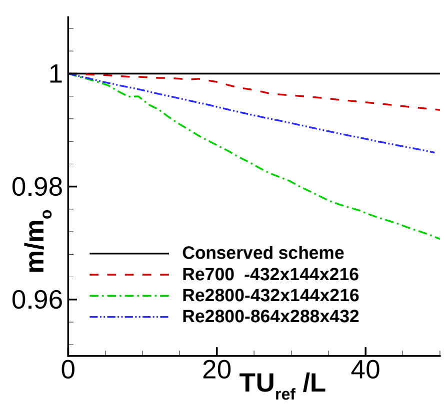

FIG. 7. Mass variations within the computational domain with and without mass correction (Re=700 and 2800)

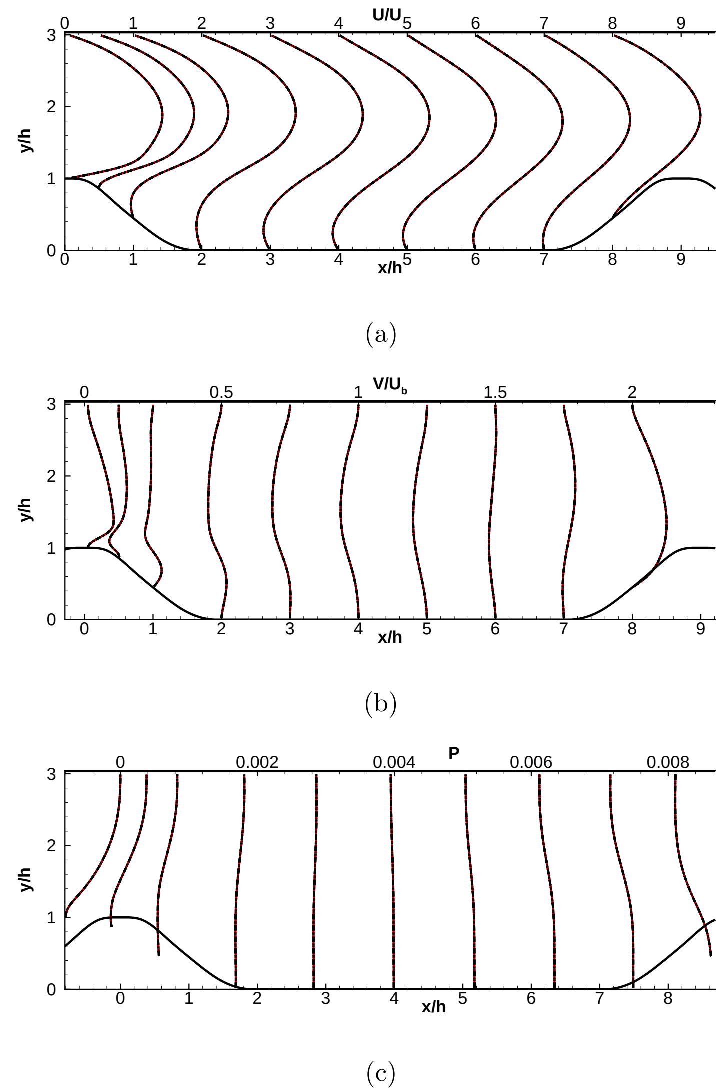

FIG. 8. Predicted velocity and pressure distributions at x/h=0.05, 0.5, 1, 2, 3, 4, 5, 6, 7 and 8. (Re=100, ———: Scheme-A; - - - - - -: Scheme-B; -·-·-·-·-: scheme-C; -··-··-··-: Scheme-D, 576×192 grid). (a) U-velocity, (b) V-velocity, (c) Pressure.

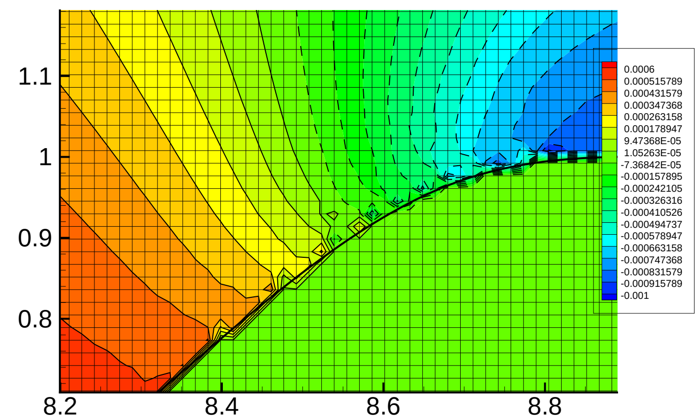

(a)

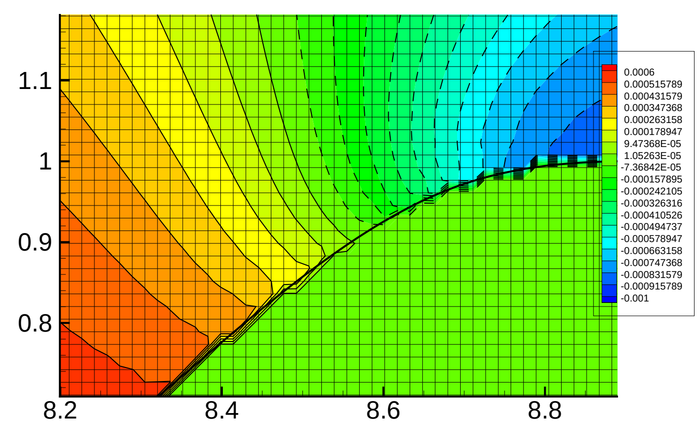

(b)

FIG. 9. Distributions of zoom-view pressure contours-Scheme-A and scheme-C (Re=100, 576×192 grid). (a) Scheme-A, (b) Scheme-C.

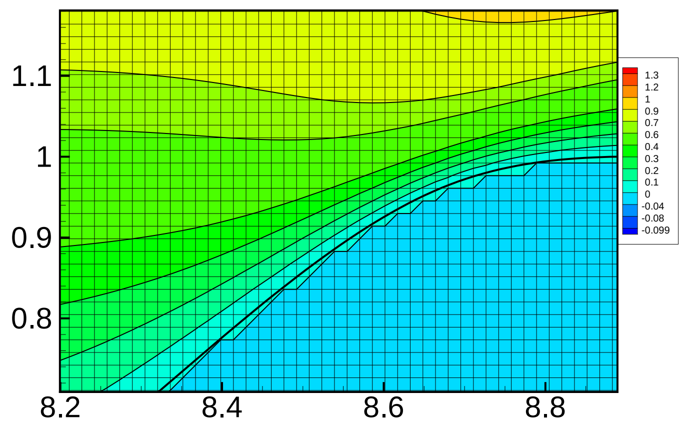

(a)

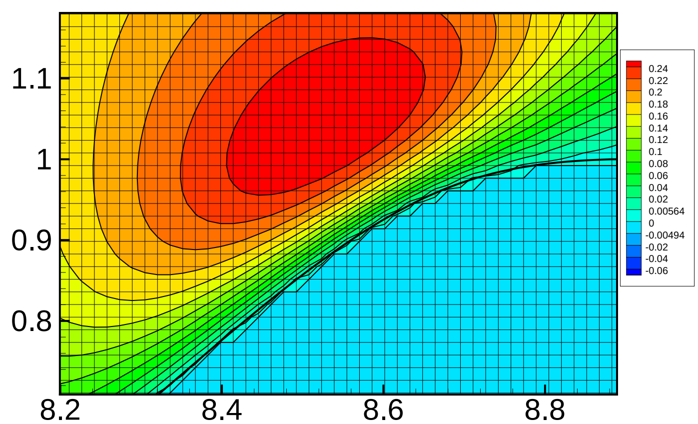

(b)

FIG. 10. Distributions of zoom-view streamwise and vertical velocity contours (Re=100, ——: Scheme-A; - - - - - -: Scheme-B; -·-·-·-·-: scheme-C; -··-··-··-: Scheme-D, 576 × 192 grid). (a) U-velocity, (b) V-velocity.

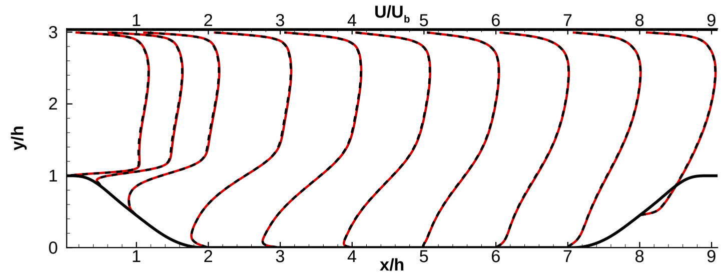

(a)

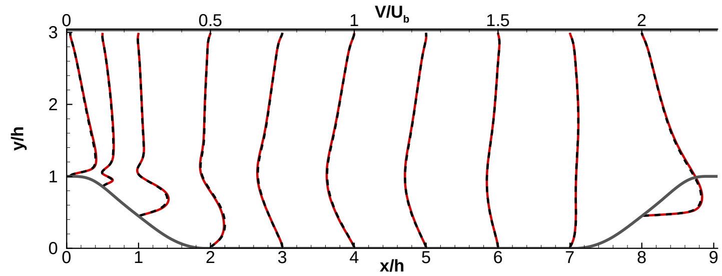

(b)

FIG. 11. Predicted mean velocity distributions at x/h=0.05, 0.5, 1, 2, 3, 4, 5, 6, 7 and 8. (Re=2800, ——: Scheme-A; - - - - - -: Scheme-C, $864 \times 288 \times 462$ grid). (a) U-velocity, (b) V-velocity.

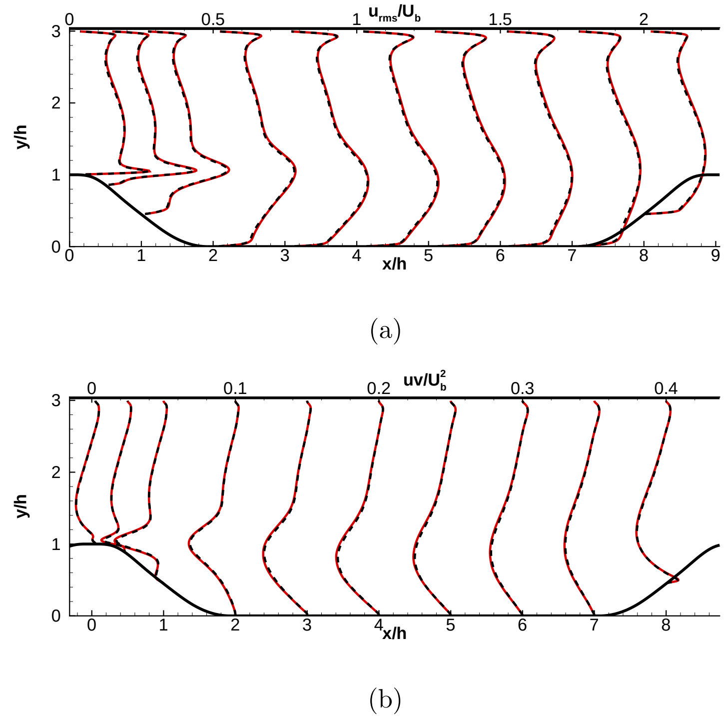

FIG. 12. Predicted turbulence distributions at x/h=0.05, 0.5, 1, 2, 3, 4, 5, 6, 7 and 8. (Re=100, ——: Scheme-A; ------: Scheme-C, $864 \times 288 \times 462$ grid). (a) Streamwise turbulence intensity, (b) Shear stress.

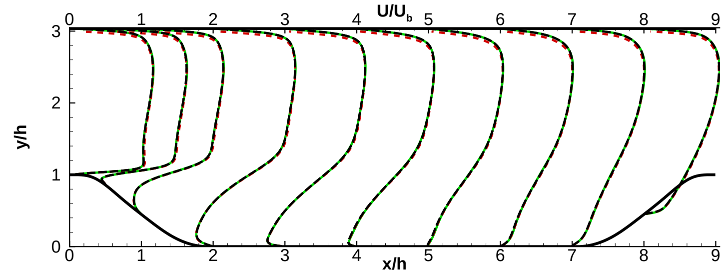

(a)

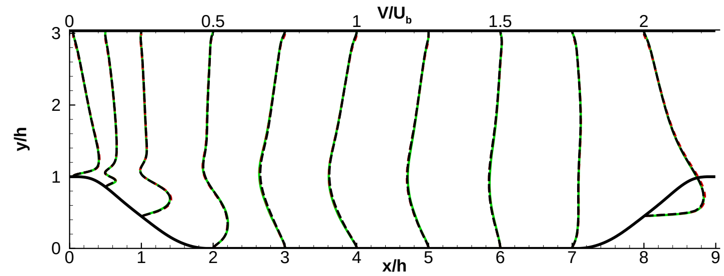

(b)

FIG. 13. Predicted mean velocity distributions at x/h=0.05, 0.5, 1, 2, 3, 4, 5, 6, 7 and 8-Re=2800. (—: Breuer et al. (2009); - - - - -: H=3h, $864 \times 288 \times 462$ grid; - - - - - -: H=3.036h, $864 \times 292 \times 462$ grid). (a) Mean streamwsie velocity, (b) Mean vertical velocity.

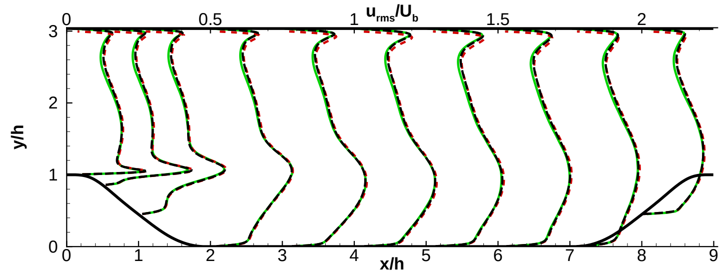

(a)

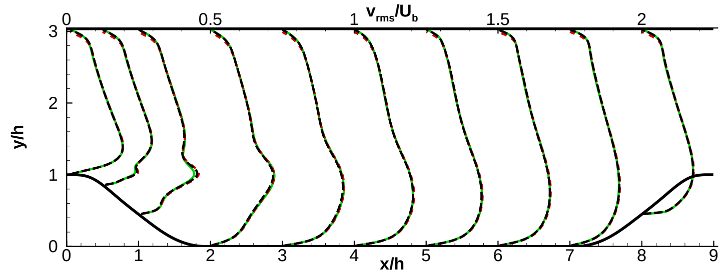

(b)

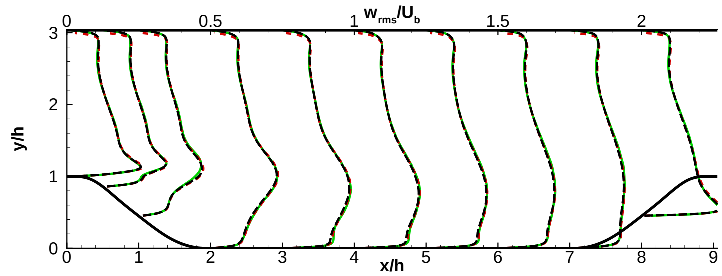

(c)

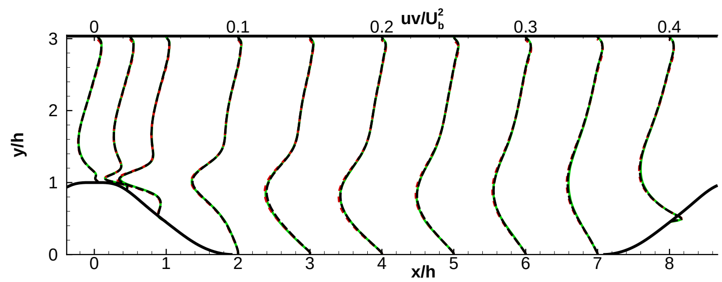

(d)

FIG. 14. Predicted turbulence intensity and shear stress distributions at x/h=0.05, 0.5, 1, 2, 3, 4, 5, 6, 7 and 8-Re=2800. (—: Breuer et al. (2009); - - - - -: H=3h, $864 \times 288 \times 462$ grid; - - - - - -: H=3.036h, $864 \times 292 \times 462$ grid). (a) Streamwise turbulence intensity, (b) Vertical turbulence intensity, (c) Spanwise turbulence intensity, (d) Shear stress.

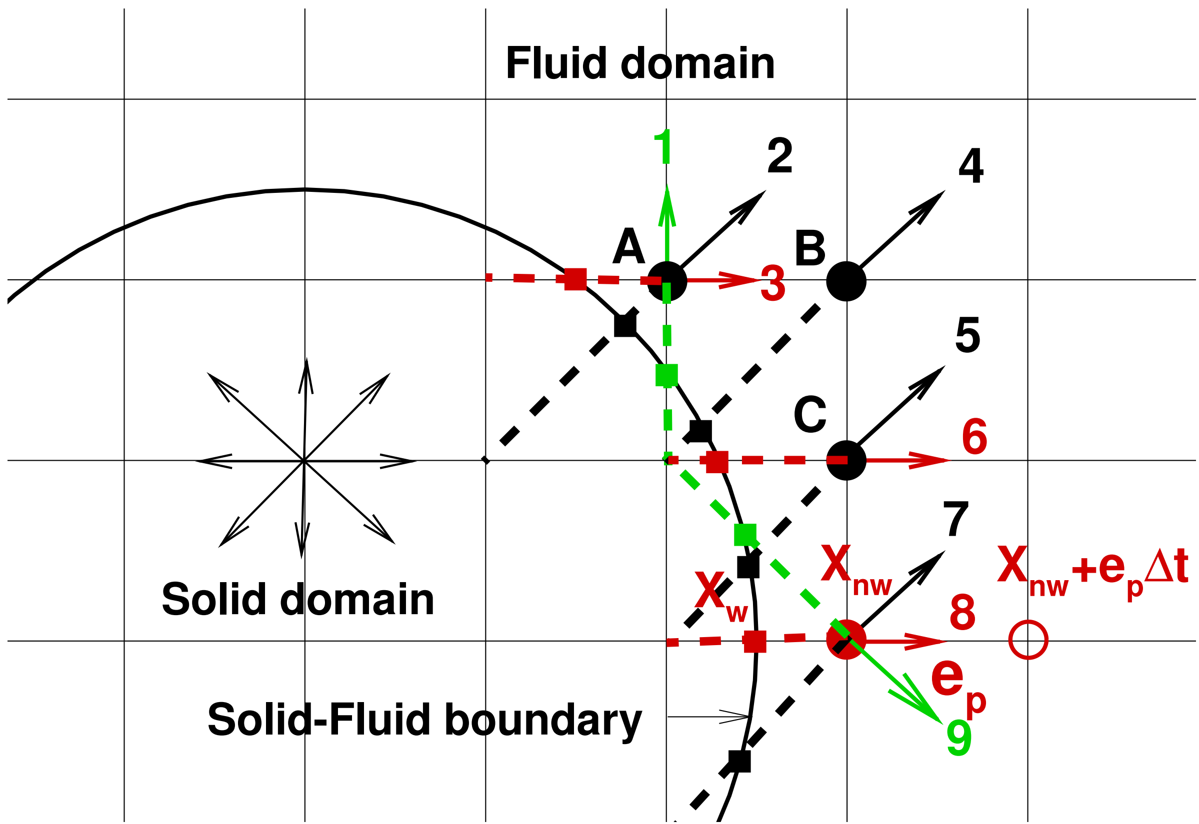

Fluid domain
1
2
4
A
B
3
5
C
6
7
X_nw
X_nw+e_pΔt
X_w
8
Solid domain
e_p
9
Solid-Fluid boundary

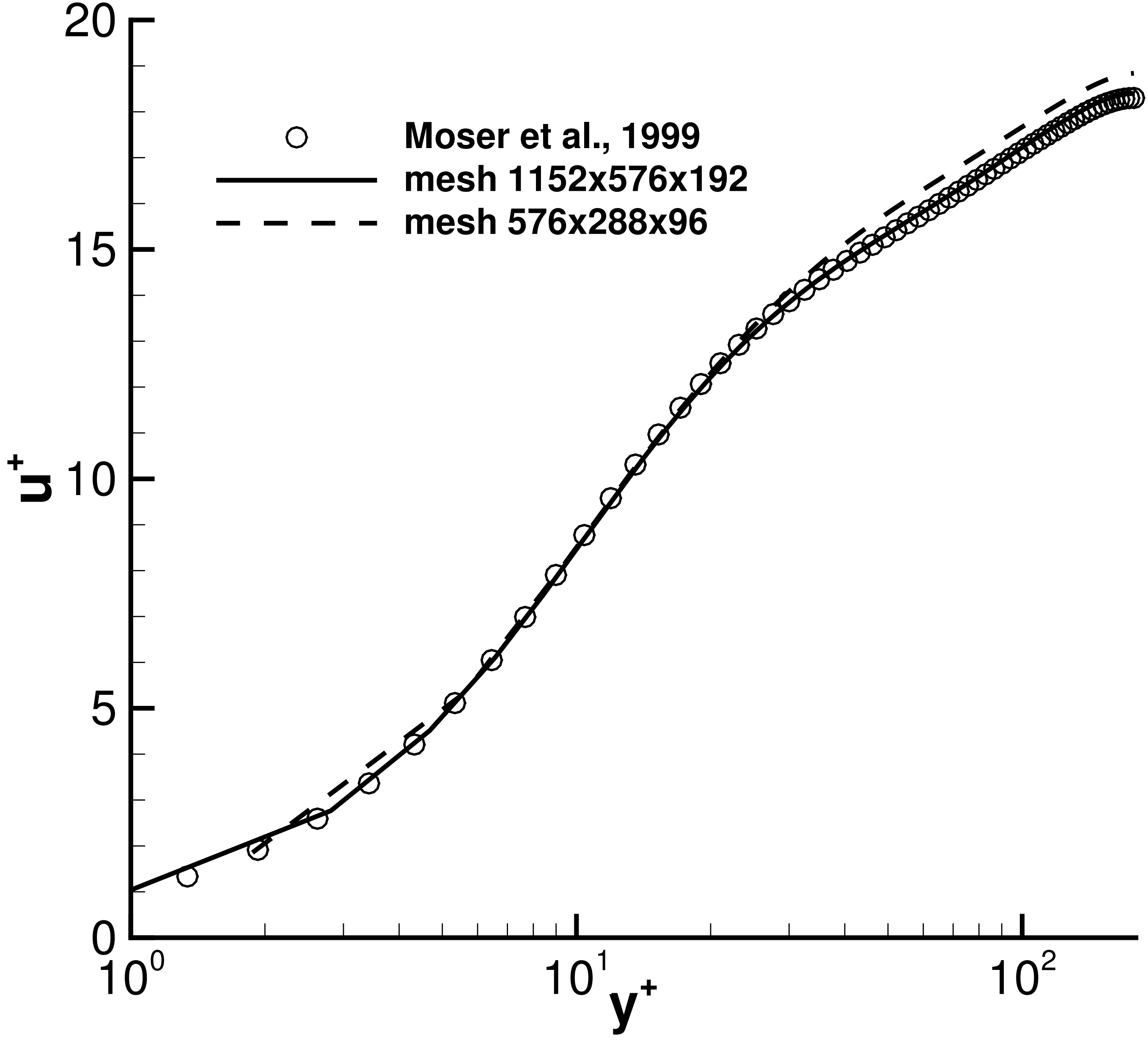

Moser et al., 1999
mesh 1152x576x192
mesh 576x288x96
u+
y+
0
5
10
15
20
10^0
10^1
10^2

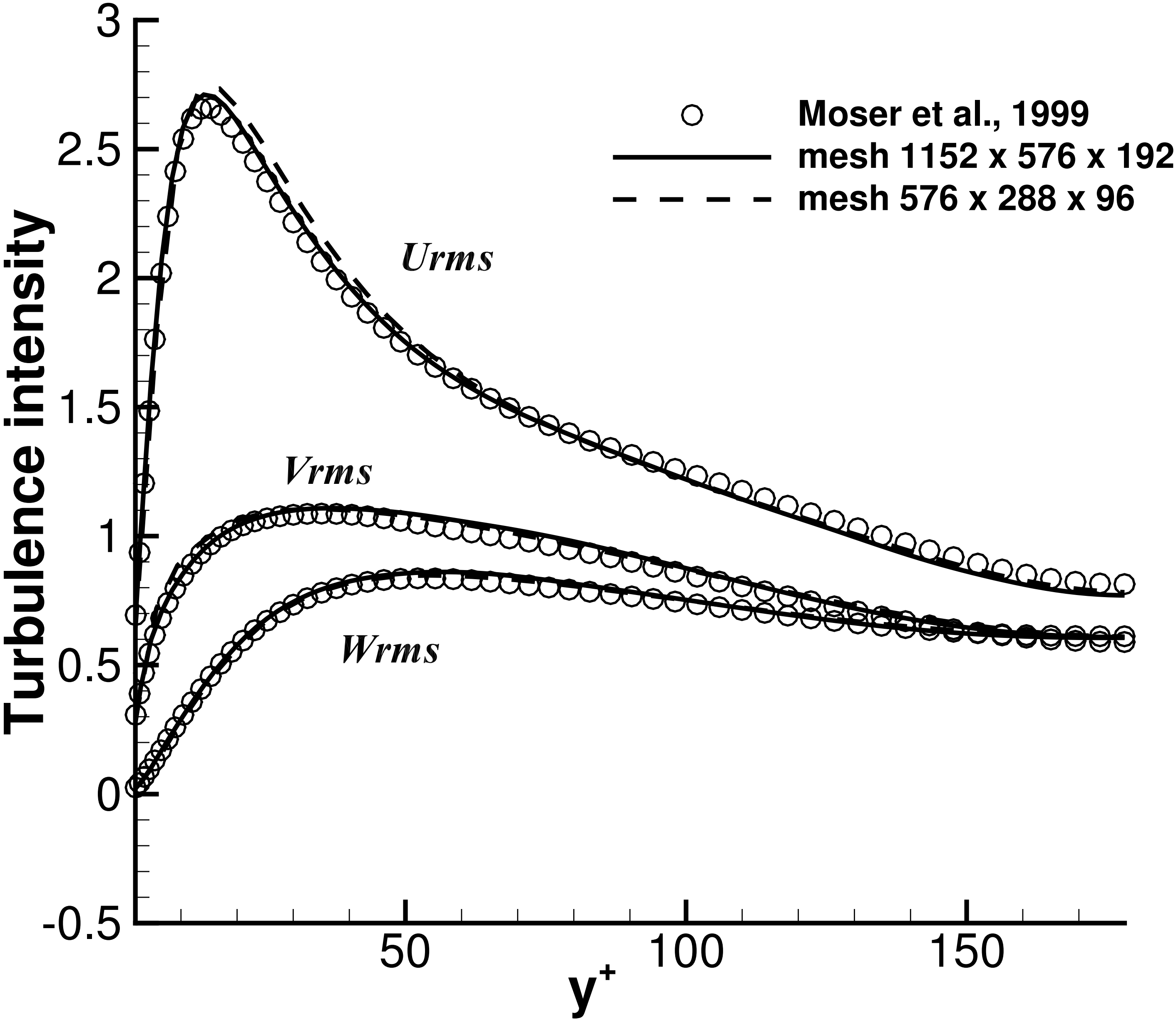

Moser et al., 1999
mesh 1152 x 576 x 192
mesh 576 x 288 x 96
Urms
Vrms
Wrms
Turbulence intensity
y+
3
2.5
2
1.5
1
0.5
0
-0.5
50
100
150

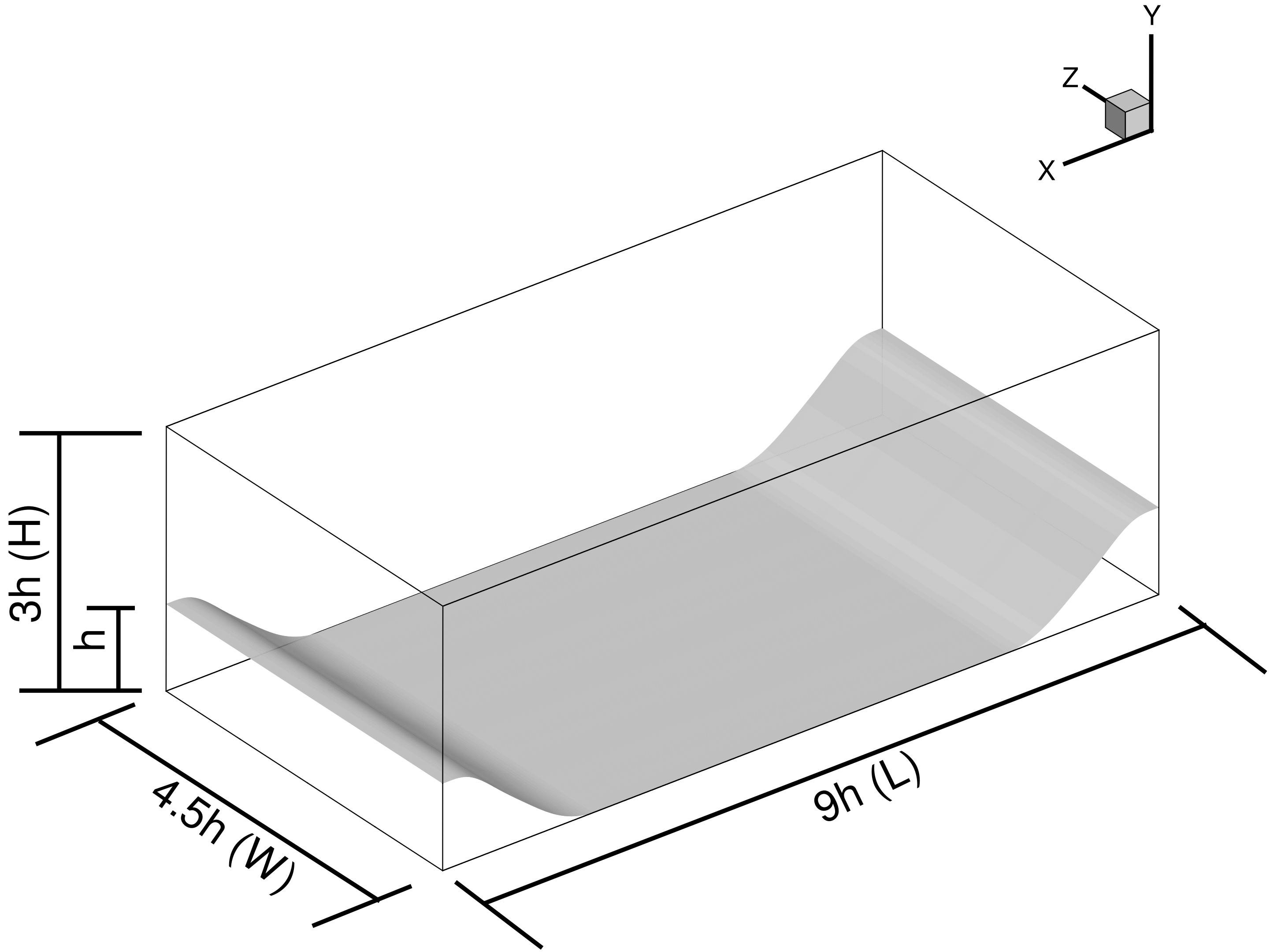

Y
Z
X
3h (H)
h
4.5h (W)
9h (L)

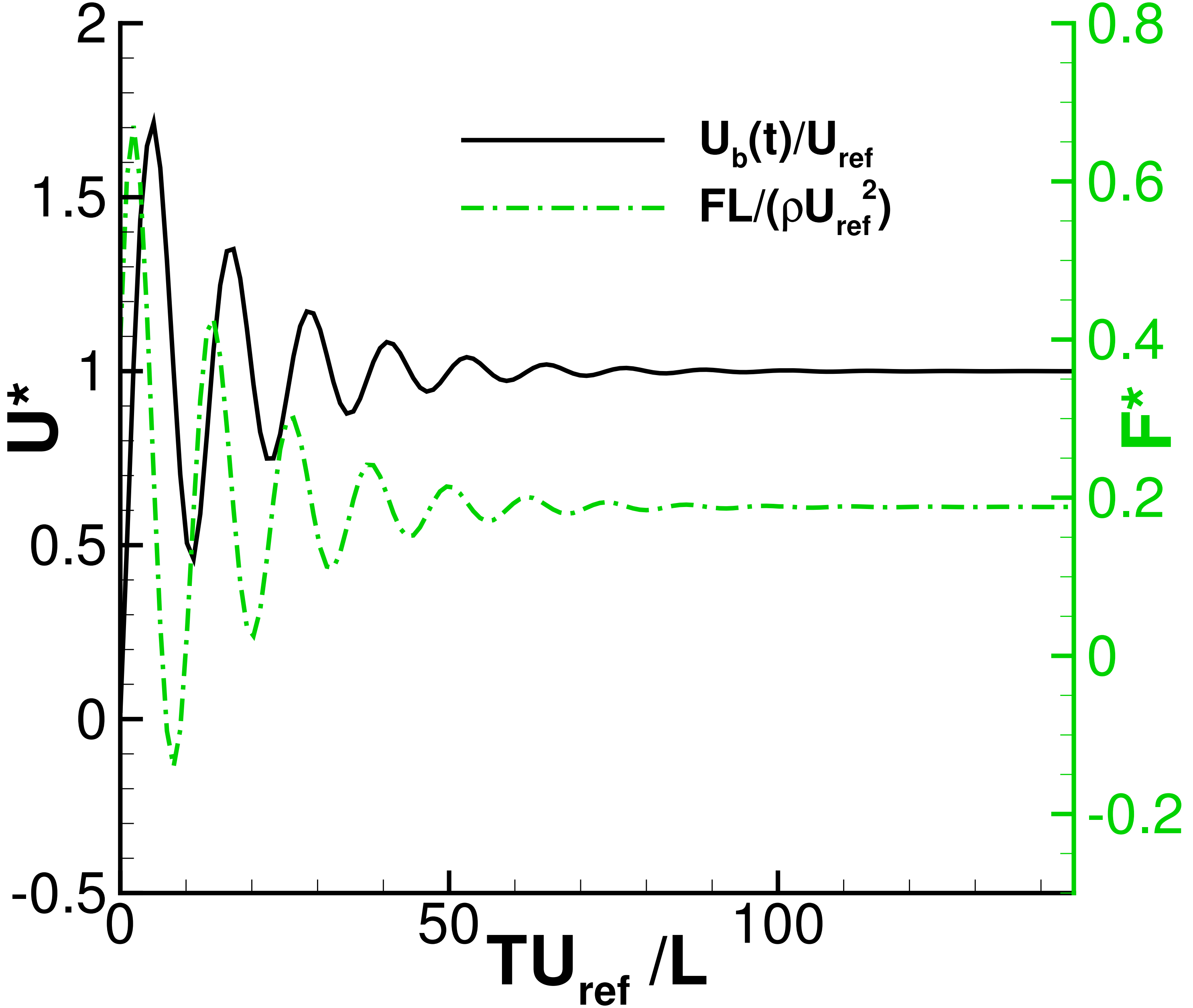

$U_b(t)/U_{ref}$
$FL/(\rho U_{ref}^2)$
U*
F*
TU_{ref}/L
2
1.5
1
0.5
0
-0.5
0.8
0.6
0.4
0.2
0
-0.2
0
50
100

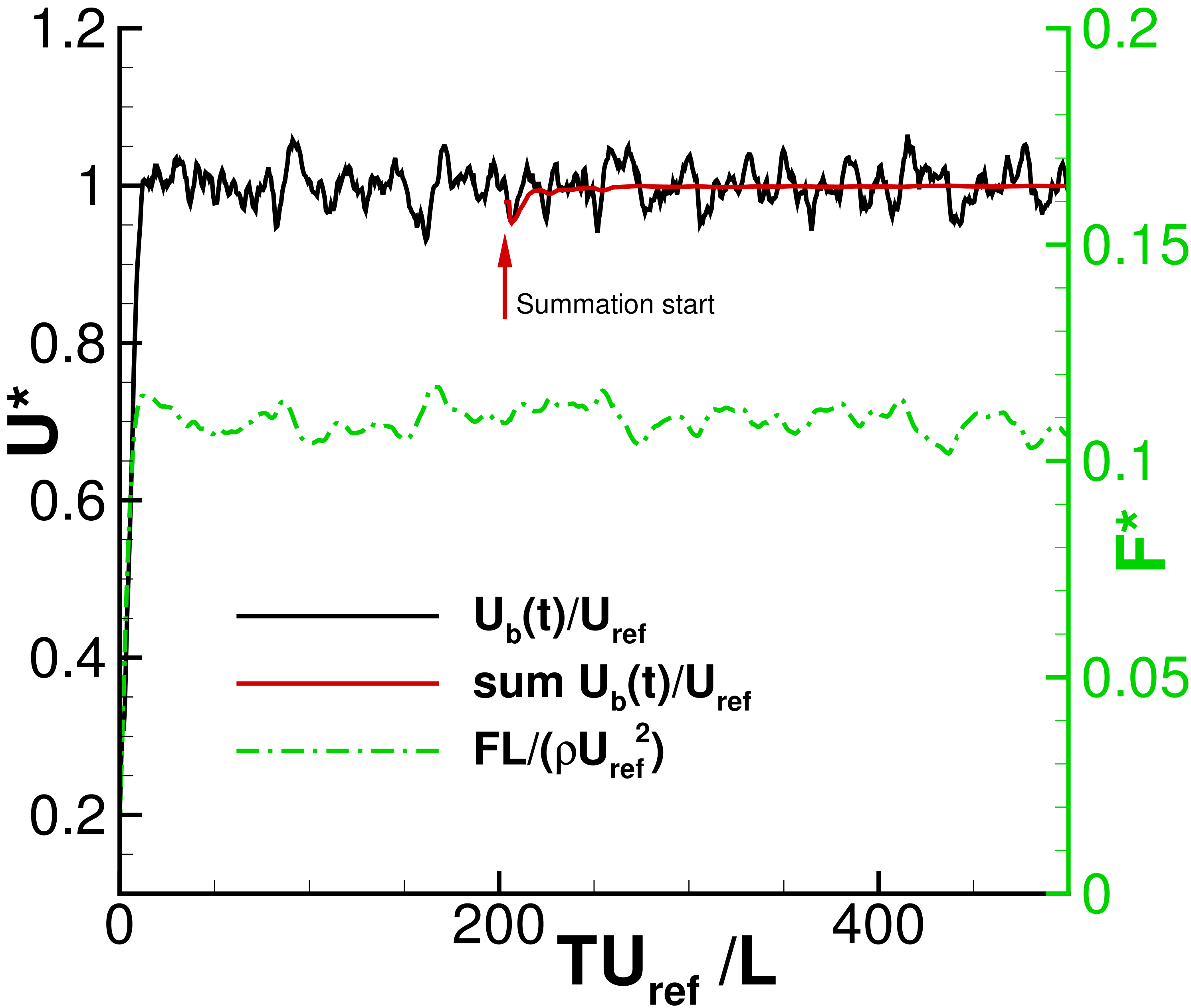

1.2
1
0.8
0.6
0.4
0.2
U*
0.2
0.15
0.1
0.05
0
F*
Summation start
U_b(t)/U_ref
sum U_b(t)/U_ref
FL/(ρU_ref^2)
0
200
400
TU_ref /L

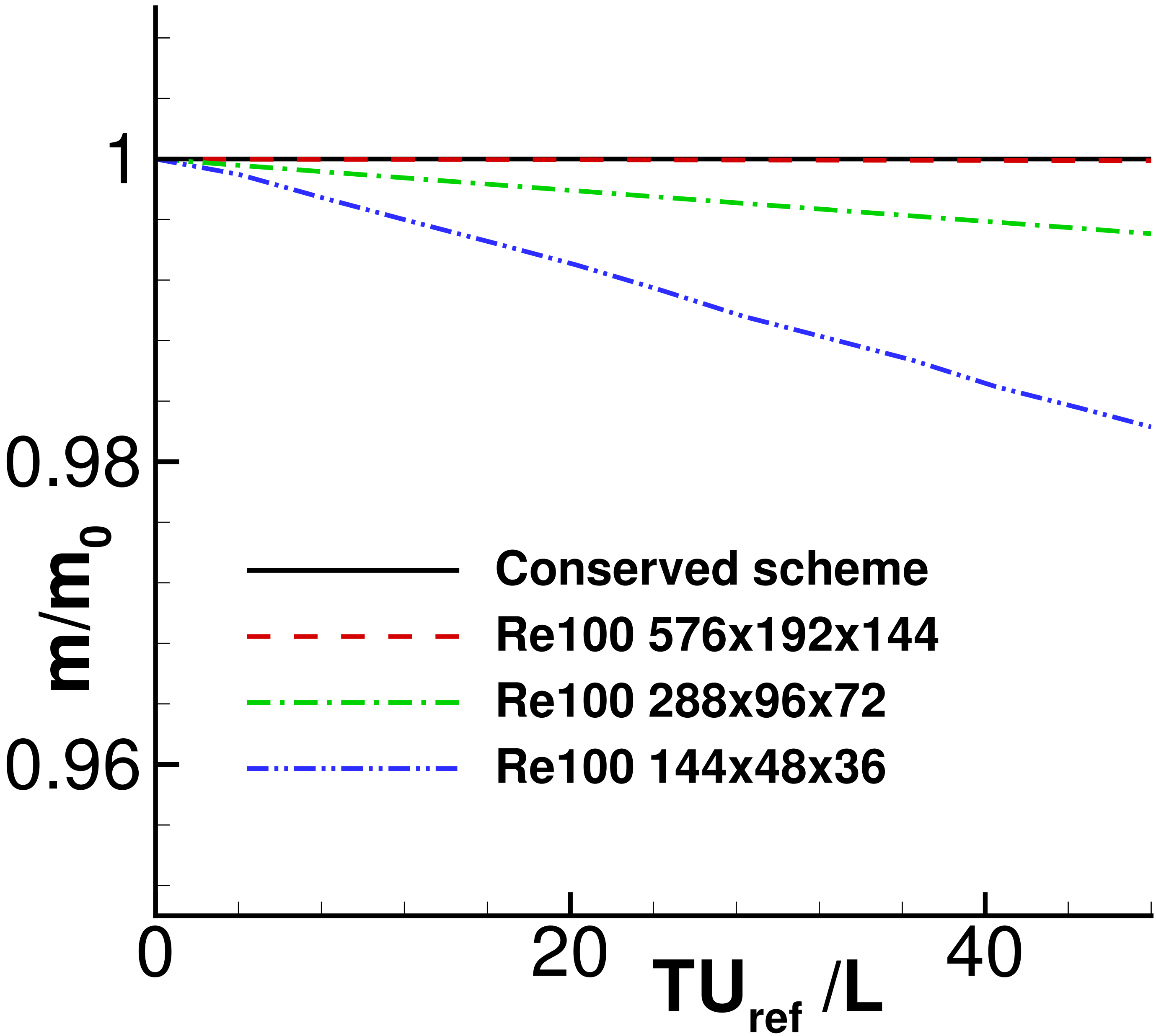

1
0.98
0.96
m/m_0
Conserved scheme
Re100 576x192x144
Re100 288x96x72
Re100 144x48x36
0
20
40
TU_{ref}/L

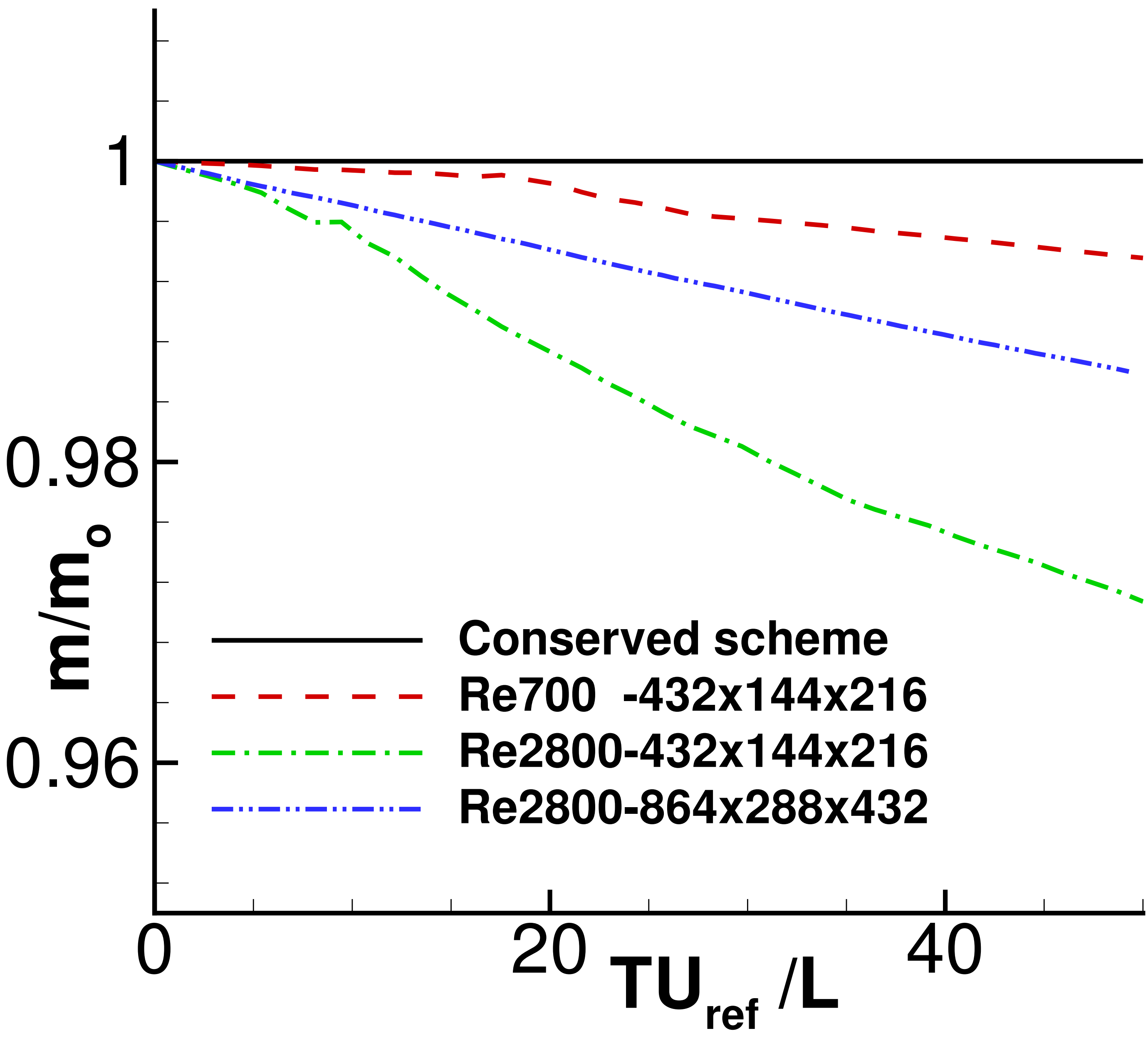

1
0.98
0.96
m/m_o
0
20
40
TU_ref /L
Conserved scheme
Re700 -432x144x216
Re2800-432x144x216
Re2800-864x288x432

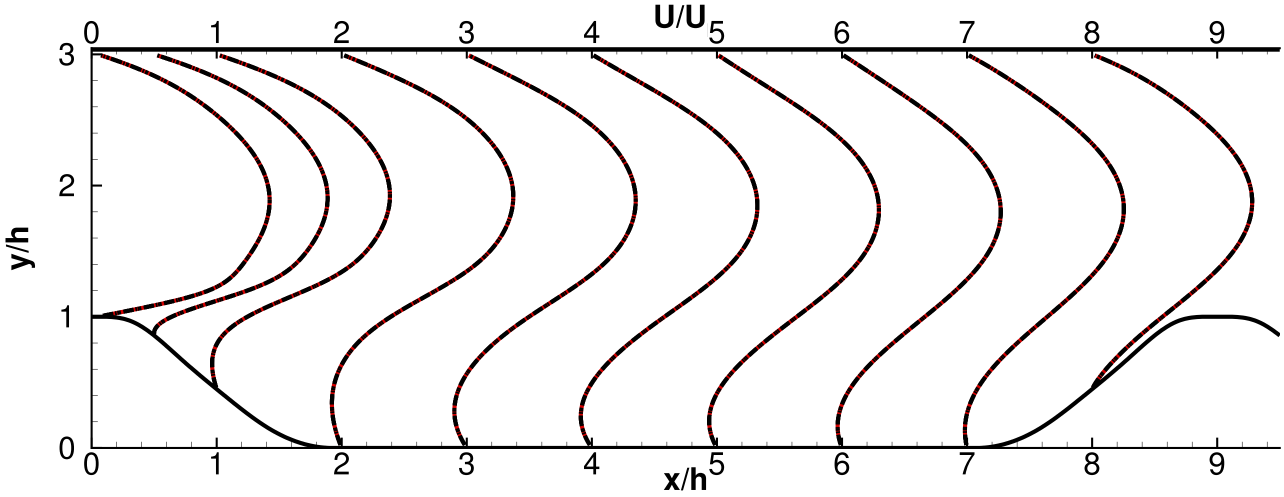
U/U
5
0 1 2 3 4 5 6 7 8 9
y/h
0 1 2 3
x/h
0 1 2 3 4 5 6 7 8 9

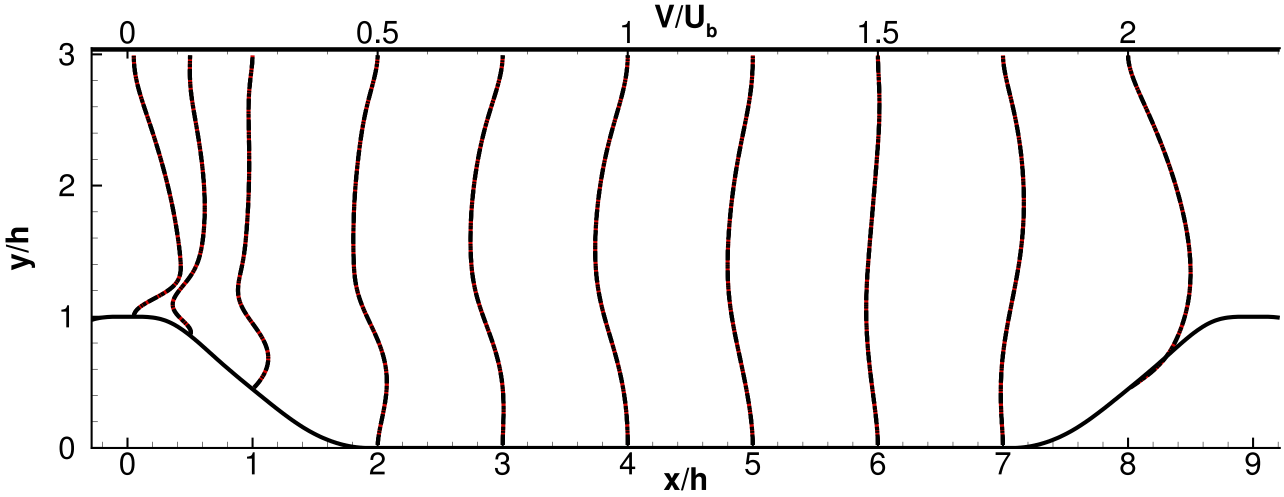

V/U_b
0
0.5
1
1.5
2
3
2
1
0
y/h
0
1
2
3
4
5
6
7
8
9
x/h

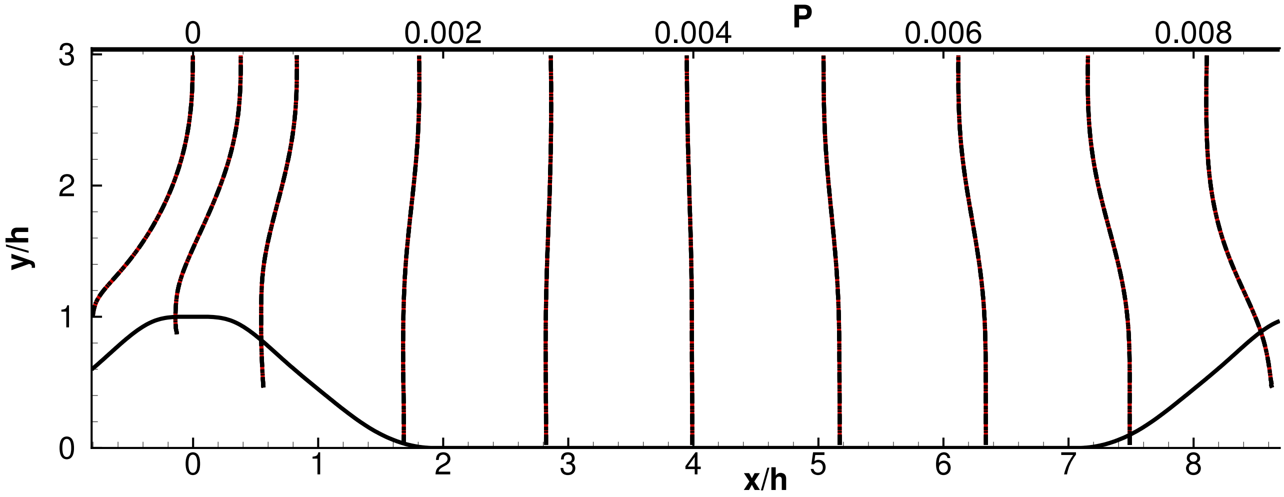
P
0
0.002
0.004
0.006
0.008
3
2
1
0
y/h
0
1
2
3
4
5
6
7
8
x/h

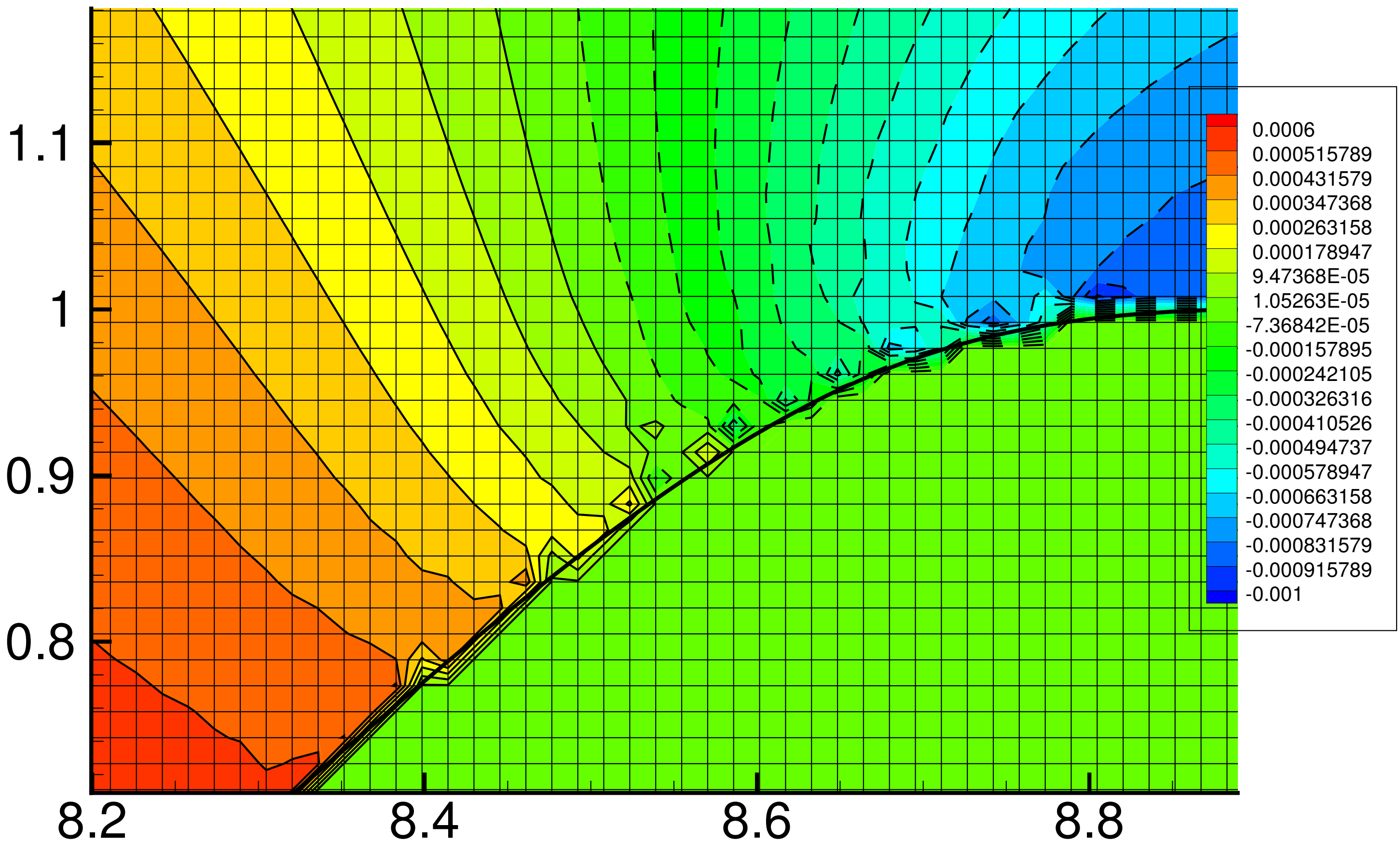
0.0006
0.000515789
0.000431579
0.000347368
0.000263158
0.000178947
9.47368E-05
1.05263E-05
-7.36842E-05
-0.000157895
-0.000242105
-0.000326316
-0.000410526
-0.000494737
-0.000578947
-0.000663158
-0.000747368
-0.000831579
-0.000915789
-0.001
1.1
1
0.9
0.8
8.2
8.4
8.6
8.8

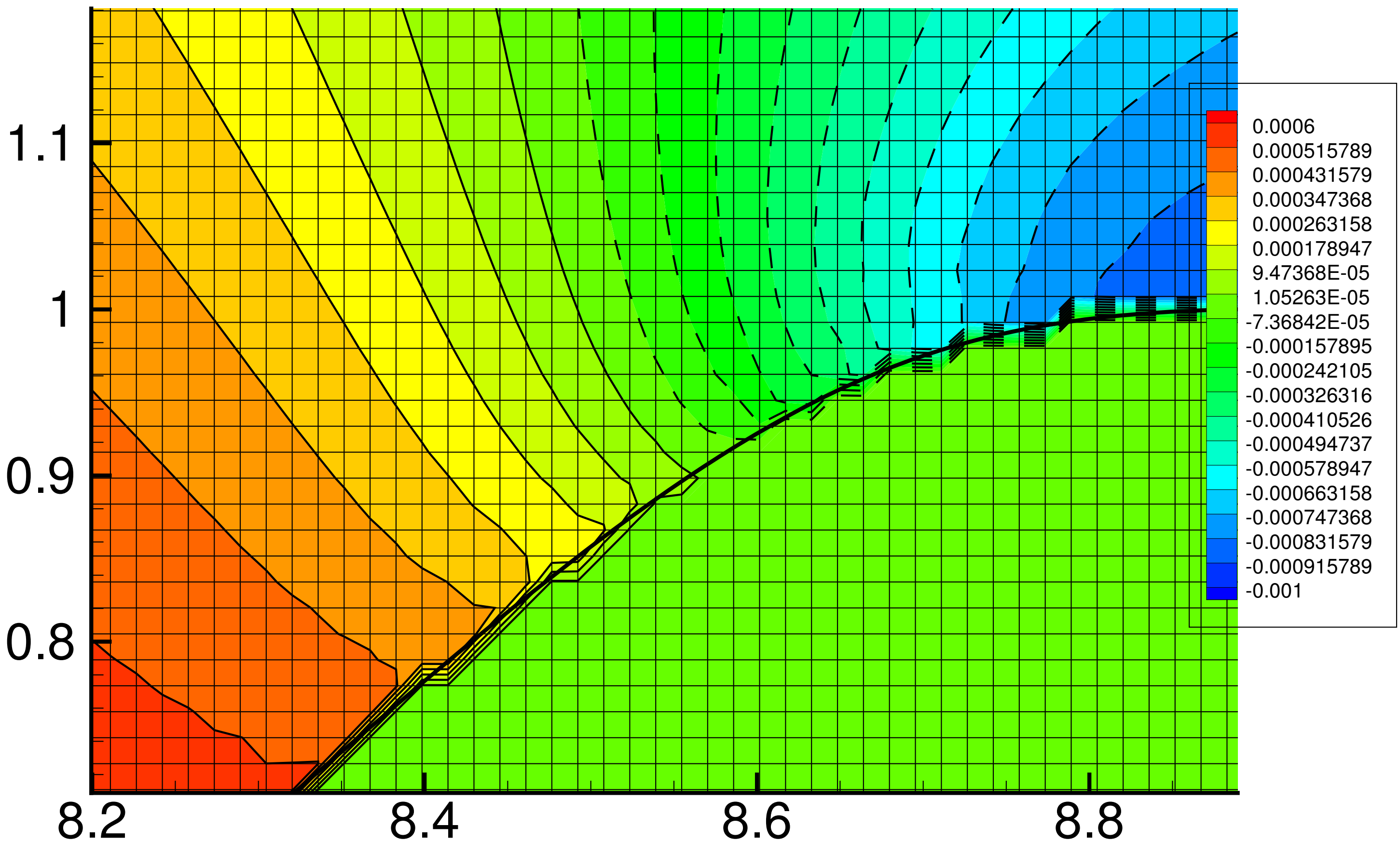

1.1
1
0.9
0.8
8.2
8.4
8.6
8.8
0.0006
0.000515789
0.000431579
0.000347368
0.000263158
0.000178947
9.47368E-05
1.05263E-05
-7.36842E-05
-0.000157895
-0.000242105
-0.000326316
-0.000410526
-0.000494737
-0.000578947
-0.000663158
-0.000747368
-0.000831579
-0.000915789
-0.001

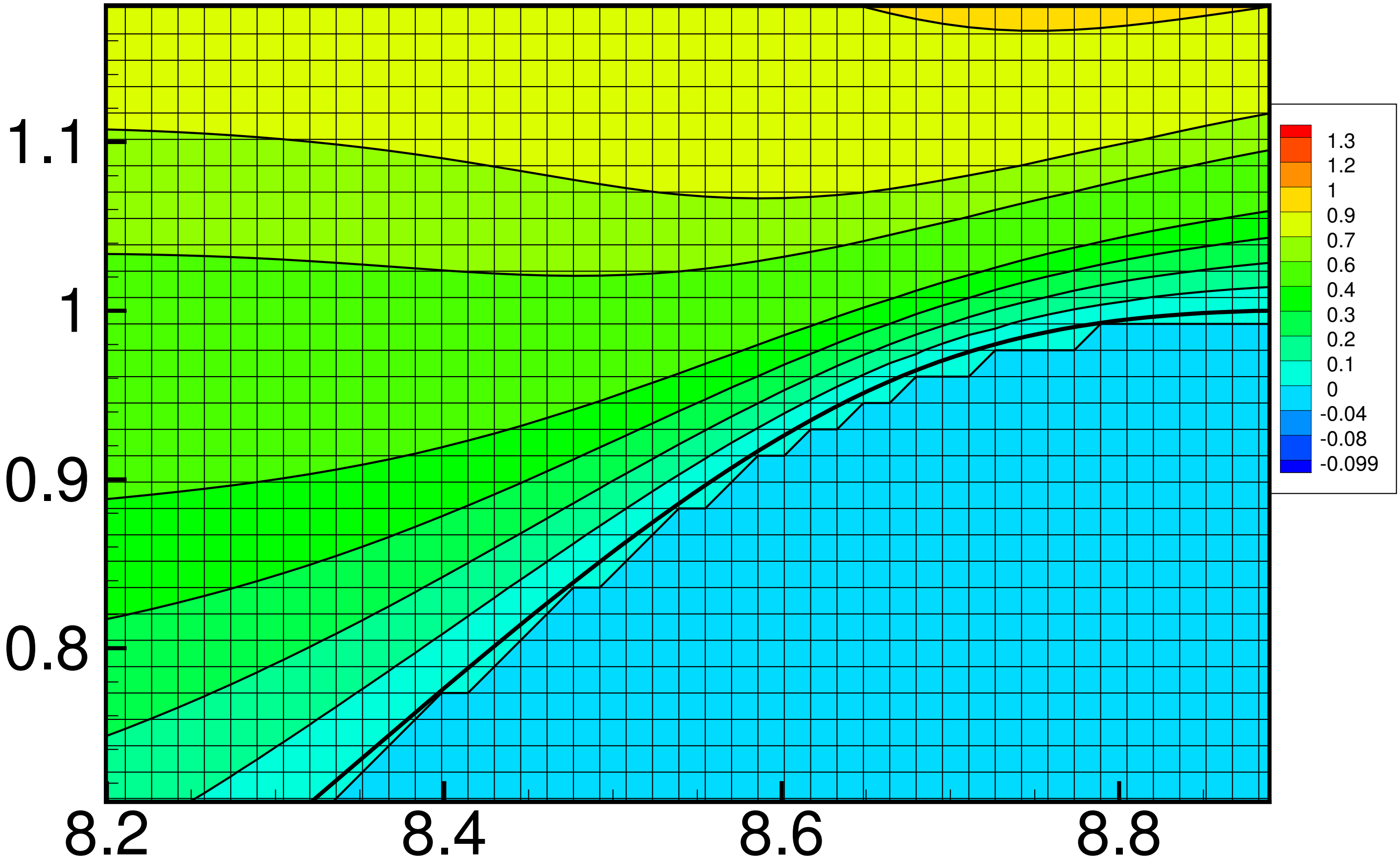
1.1
1
0.9
0.8
8.2
8.4
8.6
8.8
1.3
1.2
1
0.9
0.7
0.6
0.4
0.3
0.2
0.1
0
-0.04
-0.08
-0.099

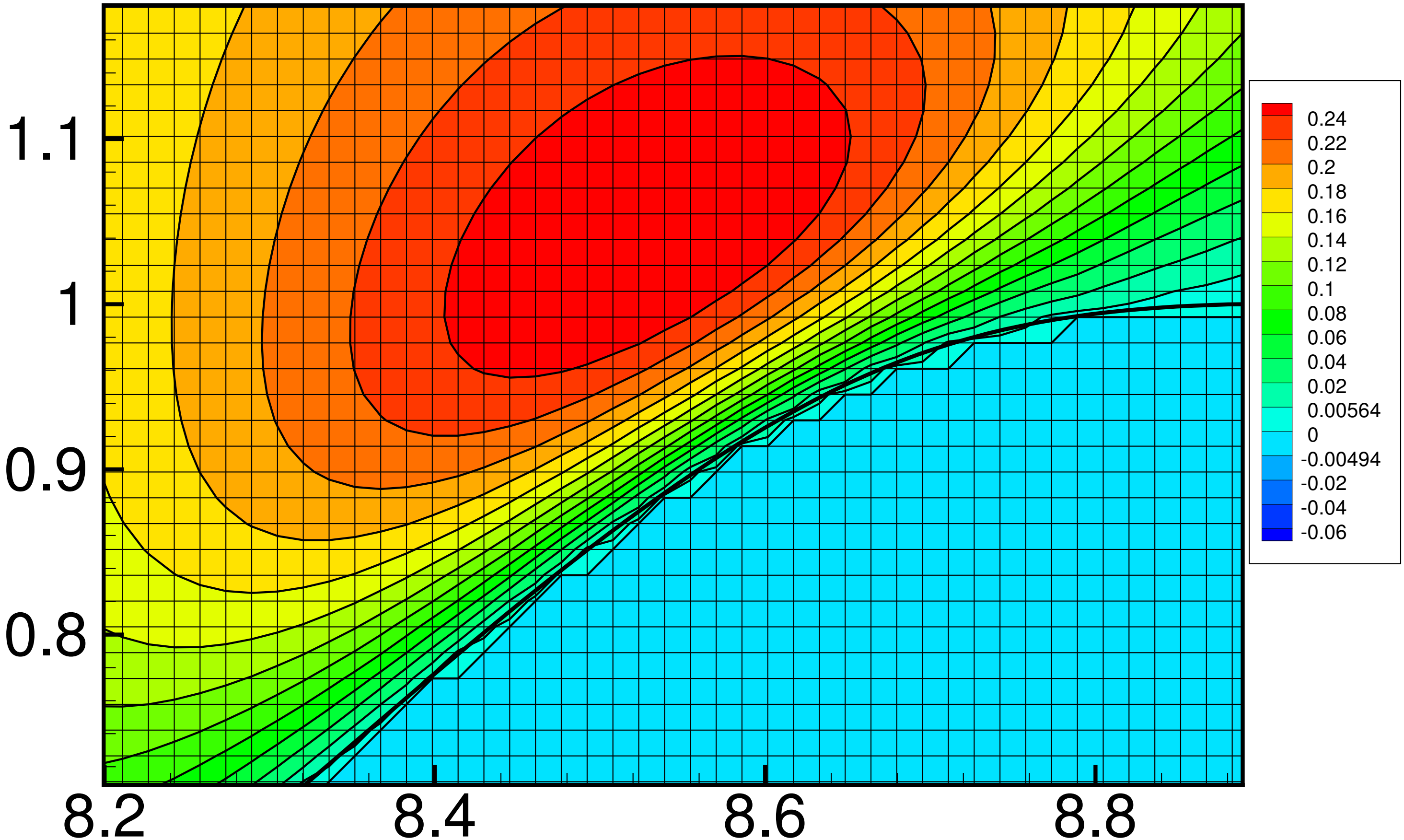
0.24
0.22
0.2
0.18
0.16
0.14
0.12
0.1
0.08
0.06
0.04
0.02
0.00564
0
-0.00494
-0.02
-0.04
-0.06
1.1
1
0.9
0.8
8.2
8.4
8.6
8.8

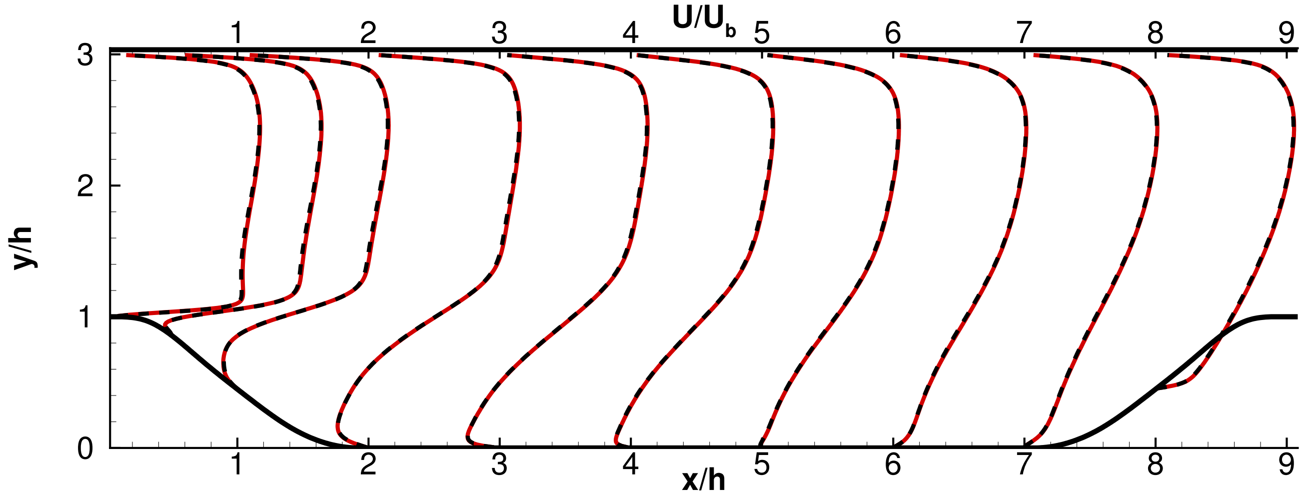
U/U_b
1 2 3 4 5 6 7 8 9
y/h
0 1 2 3
x/h
1 2 3 4 5 6 7 8 9

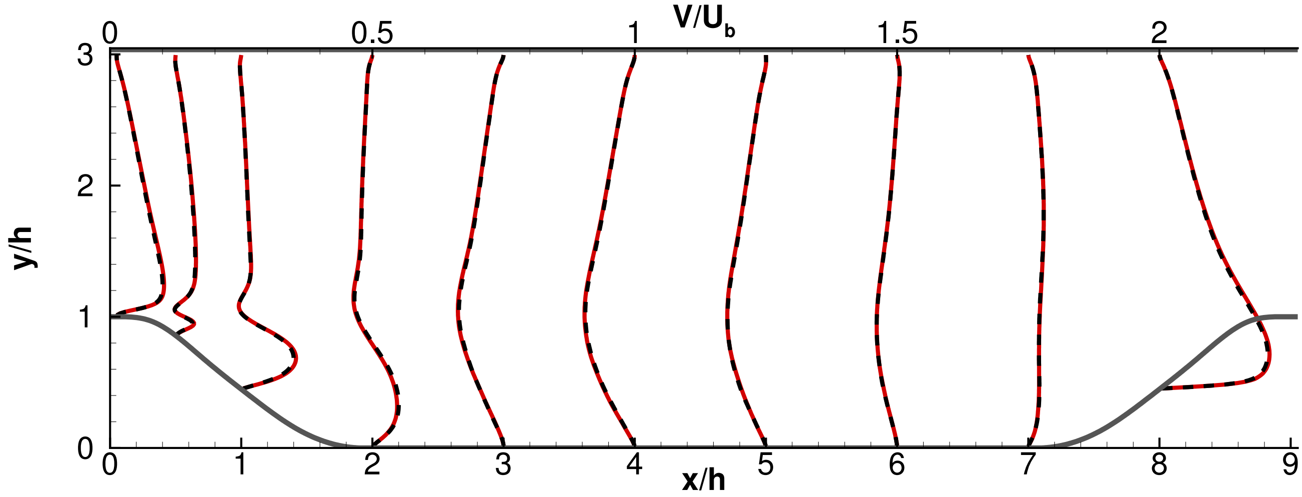

V/U_b
0
0.5
1
1.5
2
y/h
0
1
2
3
x/h
0
1
2
3
4
5
6
7
8
9

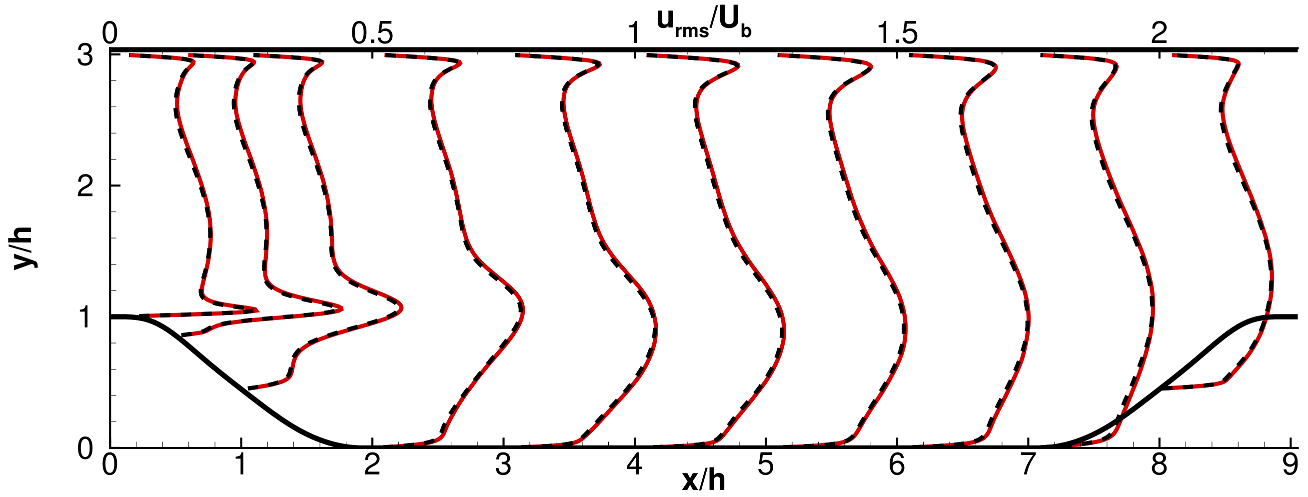

u_rms/U_b
0
0.5
1
1.5
2
y/h
0
1
2
3
x/h
0
1
2
3
4
5
6
7
8
9

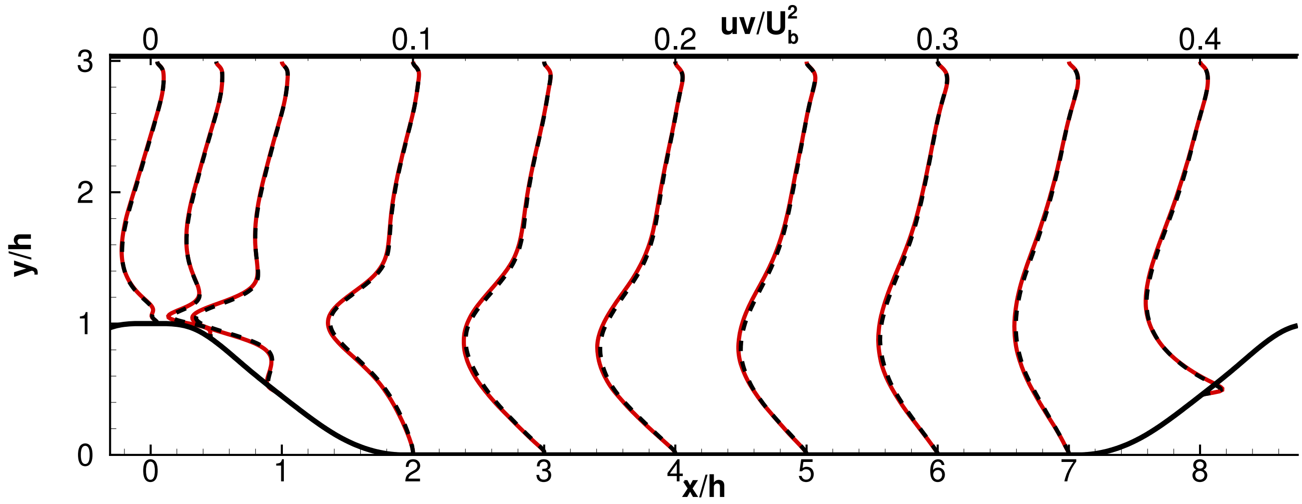
uv/U_b^2
0
0.1
0.2
0.3
0.4
y/h
0
1
2
3
x/h
0
1
2
3
4
5
6
7
8

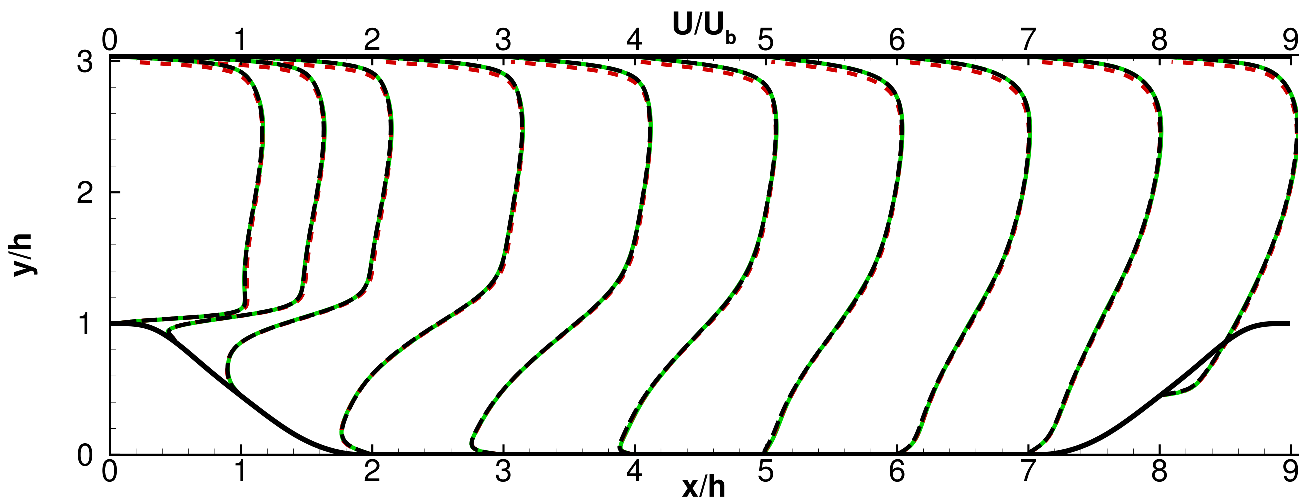

U/U_b
0 1 2 3 4 5 6 7 8 9
y/h
0 1 2 3
x/h
0 1 2 3 4 5 6 7 8 9

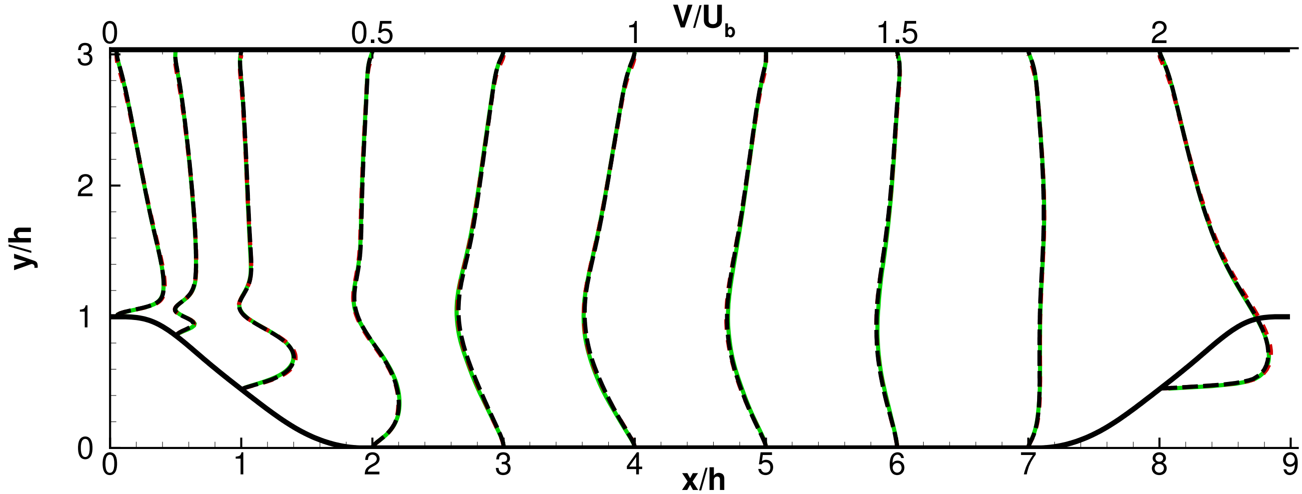
V/U_b
0
0.5
1
1.5
2
y/h
0
1
2
3
x/h
0
1
2
3
4
5
6
7
8
9

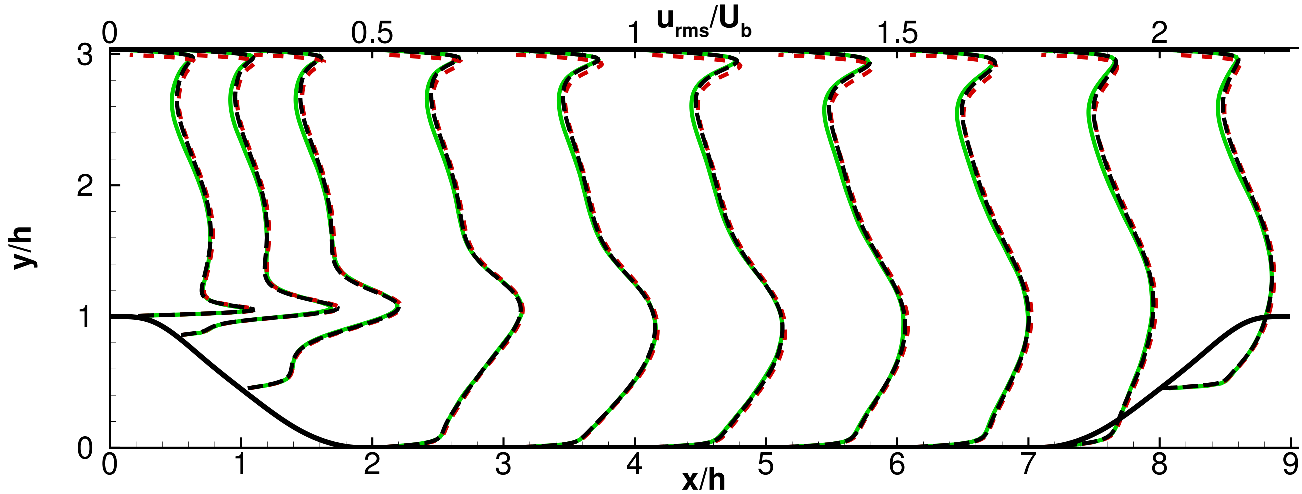

u_rms/U_b
0
0.5
1
1.5
2
y/h
3
2
1
0
x/h
0
1
2
3
4
5
6
7
8
9

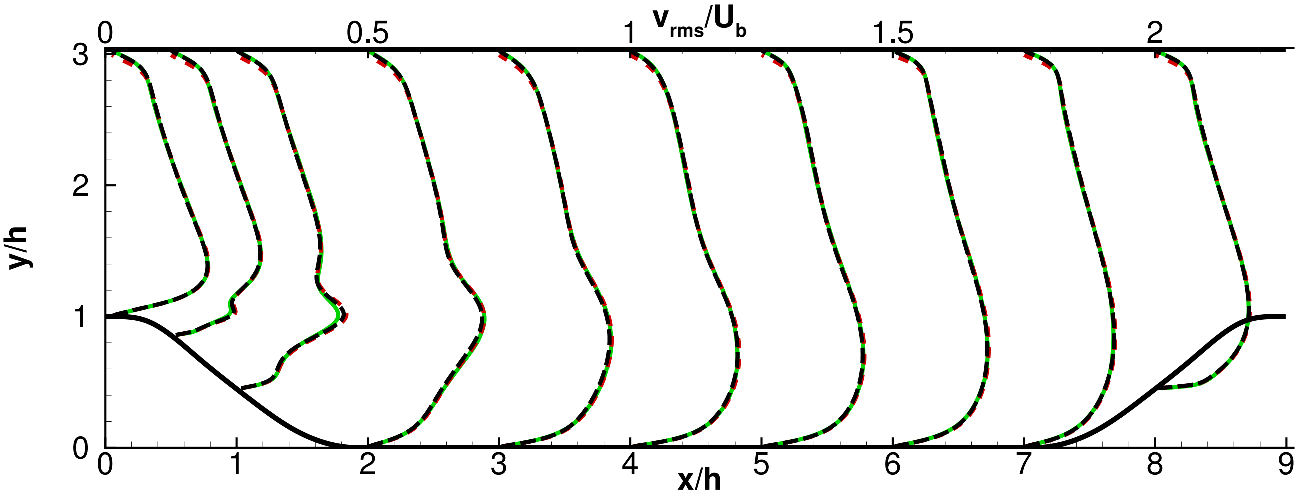

v_{rms}/U_b
0
0.5
1
1.5
2
3
2
1
0
y/h
0
1
2
3
4
5
6
7
8
9
x/h

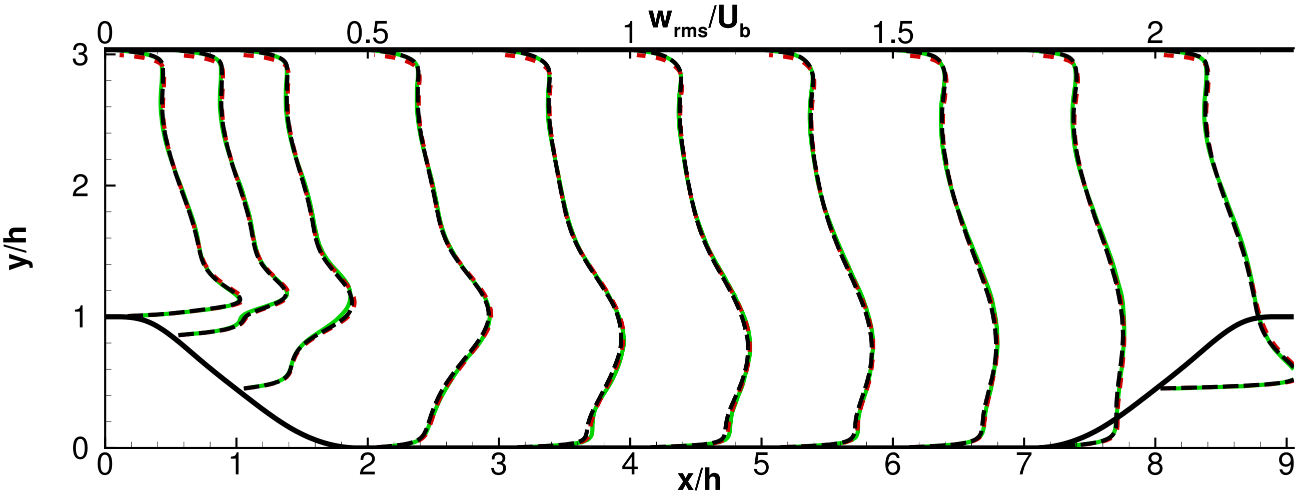

0
0.5
1
w_{rms}/U_b
1.5
2
3
2
1
0
y/h
0
1
2
3
4
5
6
7
8
9
x/h

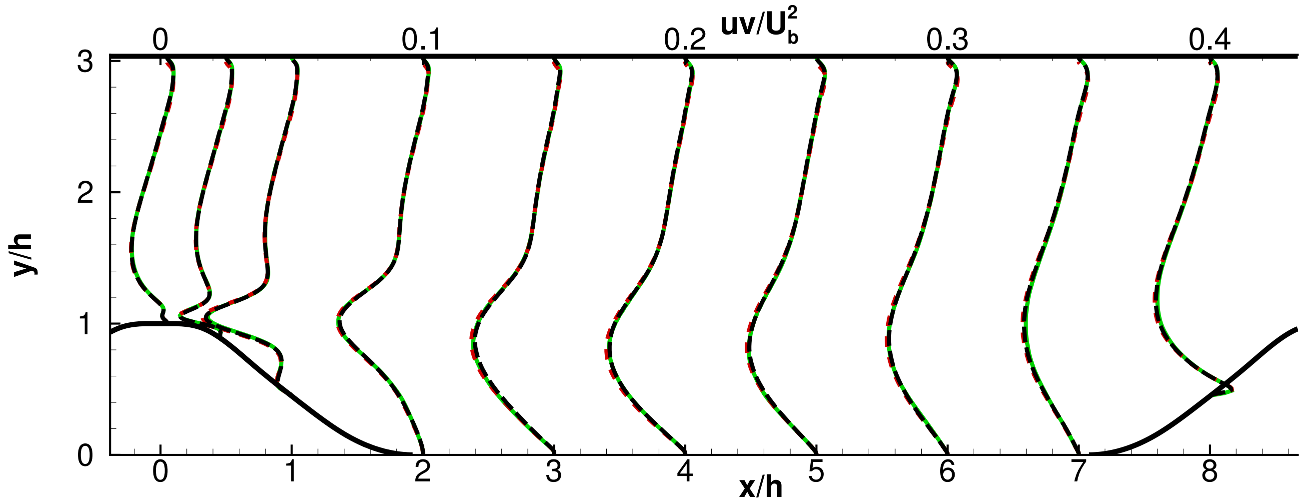

uv/U_b^2
0
0.1
0.2
0.3
0.4
3
2
1
0
y/h
0
1
2
3
4
5
6
7
8
x/h